Available online at www.sciencedirect.com

SciVerse ScienceDirect

Geochimica et Cosmochimica Acta 75 (2011) 5927–5950

Geochimica et Cosmochimica Acta

www.elsevier.com/locate/gca

Modelling Nd-isotopes with a coarse resolution ocean circulation model: Sensitivities to model parameters and source/sink distributions

Johannes Rempfer [a,b,*], Thomas F. Stocker [a,b], Fortunat Joos [a,b], Jean-Claude Dutay [c], Mark Siddall [d]

[a] Climate and Environmental Physics, Physics Institute, University of Bern, Sidlerstrasse 5, 3012 Bern, Switzerland
[b] Oeschger Centre for Climate Change Research, University of Bern, 3012 Bern, Switzerland
[c] Laboratoire des Sciences du Climat et de l'Environnement (LSCE), IPSL, CEA/UVSQ/CNRS, Orme des Merisiers, 91191 Gif sur Yvette, France
[d] Department of Earth Science, University of Bristol, Bristol, UK

Received 23 March 2011; accepted in revised form 17 July 2011; available online 2 August 2011

Abstract

The neodymium (Nd) isotopic composition (ϵ_{Nd}) of seawater is a quasi-conservative tracer of water mass mixing and is assumed to hold great potential for paleoceanographic studies. Here we present a comprehensive approach for the simulation of the two neodymium isotopes ^{143}Nd, and ^{144}Nd using the Bern3D model, a low resolution ocean model. The high computational efficiency of the Bern3D model in conjunction with our comprehensive approach allows us to systematically and extensively explore the sensitivity of Nd concentrations and ϵ_{Nd} to the parametrisation of sources and sinks. Previous studies have been restricted in doing so either by the chosen approach or by computational costs. Our study thus presents the most comprehensive survey of the marine Nd cycle to date.

Our model simulates both Nd concentrations as well as ϵ_{Nd} in good agreement with observations. ϵ_{Nd} covaries with salinity, thus underlining its potential as a water mass proxy. Results confirm that the continental margins are required as a Nd source to simulate Nd concentrations and ϵ_{Nd} consistent with observations. We estimate this source to be slightly smaller than reported in previous studies and find that above a certain magnitude its magnitude affects ϵ_{Nd} only to a small extent. On the other hand, the parametrisation of the reversible scavenging considerably affects the ability of the model to simulate both, Nd concentrations and ϵ_{Nd}. Furthermore, despite their small contribution, we find dust and rivers to be important components of the Nd cycle. In additional experiments, we systematically varied the diapycnal diffusivity as well as the Atlantic-to-Pacific freshwater flux to explore the sensitivity of Nd concentrations and its isotopic signature to the strength and geometry of the overturning circulation. These experiments reveal that Nd concentrations and ϵ_{Nd} are comparatively little affected by variations in diapycnal diffusivity and the Atlantic-to-Pacific freshwater flux. In contrast, an adequate representation of Nd sources and sinks is crucial to simulate Nd concentrations and ϵ_{Nd} consistent with observations. The good agreement of our results with observations paves the way for the evaluation of the paleoceanographic potential of ϵ_{Nd} in further model studies.

* Corresponding author at: Climate and Environmental Physics, Physics Institute, University of Bern, Sidlerstrasse 5, 3012 Bern, Switzerland. Tel.: +41 (0)31 631 4467; fax: +41 (0)31 631 8742.
E-mail address: rempfer@climate.unibe.ch (J. Rempfer).

0016-7037/$ - see front matter © 2011 Elsevier Ltd. All rights reserved.
doi:10.1016/j.gca.2011.07.044

1. INTRODUCTION

Adequate circulation tracers are needed for the reconstruction of past changes in ocean circulation, and considerable effort has therefore been put into the investigation of the oceanic cycling of various elements, as well as elemental and isotopic ratios, such as $\delta^{13}C$, $\delta^{18}O$, Pa/Th, Cd/Ca, and ϵ_{Nd} (see Lynch-Stieglitz, 2003, for an overview). The cycling of some of these tracers, however is affected not only by ocean circulation but also by other factors such as biological processes, and the nature and magnitude of sources. Thus the interpretation of observed variations in sediment cores, often is not unequivocal.

For the investigation of past changes in ocean circulation, there is a need for a circulation tracer whose sources and sinks are well understood and which is at best only minimally affected by biological processes. At least the latter seems to be true for the isotopic composition of neodymium (ϵ_{Nd}, Eq. (1), Goldstein and Hemming, 2003) and thus, in recent years, ϵ_{Nd} has increasingly been used in paleoceanographic studies (e.g., Frank, 2002; Frank et al., 2002; Piotrowski et al., 2004; Gutjahr et al., 2008; Pahnke et al., 2008; Piotrowski et al., 2008,Piotrowski et al., 2009; Roberts et al., 2010). However, to date the knowledge of the nature and magnitude of sources and sinks and consequently the cycling of Nd in the ocean is insufficient, complicating the application of ϵ_{Nd} as a reliable paleoceanographic tracer (Tachikawa et al., 1999; Goldstein and Hemming, 2003; Tachikawa et al., 2003; Siddall et al., 2008; Arsouze et al., 2009).

The purpose of this study therefore is to extend earlier modelling efforts of Nd-isotopes, ^{143}Nd and ^{144}Nd (Arsouze et al., 2009; Siddall et al., 2008), by presenting a comprehensive sensitivity study of the dissolved concentration of Nd ($[Nd]_d$ in pico moles per kg seawater, pmol kg^{-1}) and ϵ_{Nd} in seawater to different parametrisations of the sources and the internal cycling, as well as to the strength and geometry of the oceanic overturning circulation. This, together with new insight that will be provided by the GEOTRACES international program (SCOR Working Group, 2007), will allow us to further constrain the nature and the magnitude of the sources and sinks of Nd and thus improve our understanding of the marine Nd cycle.

For the simulation of Nd isotopes we use an approach that is similar to Siddall et al., 2008 and Arsouze et al., 2009. Though, compared to Siddall et al., 2008, our approach is more comprehensive as we explicitly define different Nd sources and also explicitly calculate biogenic particle fluxes (similar to Arsouze et al., 2009). On the other hand, and in contrast to Arsouze et al. (2009), we use a highly cost-efficient model and thus are able to run a large number of experiments. Mainly these improvements allow us to extensively and systematically explore sensitivities of Nd concentrations and ϵ_{Nd} in seawater to model parameters and source/sink distributions. Our approach thus allows for a more comprehensive survey of the marine Nd cycle, and will further our understanding of the marine Nd cycle.

The Nd isotopic ratio relative to a standard is reported as

$$\epsilon_{Nd} = \left(\frac{(^{143}Nd/^{144}Nd)_{sample}}{(^{143}Nd/^{144}Nd)_{std}} - 1 \right) \times 10^4, \quad (1)$$

where $(^{143}Nd/^{144}Nd)_{std}$ corresponds to the "bulk earth" standard value of 0.512638 (Jacobsen and Wasserburg, 1980).

$[Nd]_d$ and ϵ_{Nd} behave differently in the ocean: In the Atlantic basin ϵ_{Nd} covaries with salinity (von Blanckenburg, 1999), and is assumed to be quasi-conservative in the interior of the ocean, thus tracing mixing and origin of water masses (Piepgras and Wasserburg, 1987; Jeandel, 1993; Goldstein and Hemming, 2003). Two major endmembers are distinguished: the North Atlantic and the North Pacific. Old continental crust with low, i.e., unradiogenic, ϵ_{Nd} ($\epsilon_{Nd} < -20$) dominates in the North Atlantic region. Young volcanic material with high, i.e., radiogenic, ϵ_{Nd} (ϵ_{Nd} up to +10) can be found in the North Pacific region. Consequently, in seawater, ϵ_{Nd} is low in North Atlantic Deep Water (NADW, $\epsilon_{Nd} = -13.5 \pm 0.5$ Piepgras and Wasserburg, 1987), and reaches relatively high values in the North Pacific ($\epsilon_{Nd} = -3$, Piepgras and Jacobsen, 1988). ϵ_{Nd} is intermediate in the Indian Ocean and the Antarctic Circumpolar Current (Goldstein and Hemming, 2003, and references therein). In contrast, $[Nd]_d$ shows non-conservative, nutrient-like behavior comparable to e.g., silicate. $[Nd]_d$ increases with depth and along the circulation pathway, indicating some internal cycling of Nd (Bertram and Elderfield, 1993). Modelling studies (Bertram and Elderfield, 1993; Siddall et al., 2008; Oka et al., 2009; Arsouze et al., 2009) show that such a pattern can be simulated successfully by parametrising internal cycling using the reversible scavenging approach based on Bacon and Anderson (1982), Henderson et al. (1999), and Siddall et al. (2005). The decoupling of $[Nd]_d$ and ϵ_{Nd} becomes particularly obvious in South Atlantic "zig-zag-profiles", where ϵ_{Nd} shows large heterogeneity within single profiles, thus distinguishing southward flowing North Atlantic Deep Water (NADW) from northward flowing Antarctic Intermediate Water (AAIW) and Antarctic Bottom Water (AABW), while $[Nd]_d$ almost linearly increases with increasing depth (Jeandel, 1993; Goldstein and Hemming, 2003, Fig. 7).

Although it is accepted that all the Nd is introduced into seawater by weathering of the continental rocks surrounding the ocean basins (Goldstein and Hemming, 2003; Lynch-Stieglitz, 2003), the nature and magnitude of its sources is still a matter of debate (Elderfield and Sholkovitz, 1987; Goldstein and Jacobsen, 1987; Elderfield et al., 1990; Bertram and Elderfield, 1993; Jeandel et al., 1995; Tachikawa et al., 2003; van de Flierdt et al., 2004; Lacan and Jeandel, 2005; Arsouze et al., 2009). The total flux of Nd from dust and riverine input is estimated to be $\approx 1 \times 10^9$ g Nd yr^{-1}. Using this value and assuming a global inventory of 5.6×10^{12} g Nd (Jeandel et al., 1995), Tachikawa et al., 1999 estimated a mean residence time (τ_{Nd}) of 5000 yr. Instead, the pronounced interbasin gradient of ϵ_{Nd} rather indicates an oceanic τ_{Nd} on the order of the ocean mixing time (about 1000 yr, Broecker and Peng, 1982), and thus a mass balance problem is indicated (e.g.,

Bertram and Elderfield, 1993; Jeandel et al., 1995; Tachikawa et al., 2003; Goldstein and Hemming, 2003).

Tachikawa et al., 2003, and more recently also Arsouze et al., 2009, showed that input from rivers and dust are insufficient to simulate the distribution of ϵ_{Nd} and $[Nd]_d$. Using a 10-box-model, Tachikawa et al., 2003 detected a missing flux of 8×10^9 g Nd yr^{-1}, and proposed the continental margin as "missing source". The continental margins and their potential to serve as additional sources of Nd, have since then been subject to some discussion in the literature (e.g., van de Flierdt et al., 2004; Lacan and Jeandel, 2005; Arsouze et al., 2007; Johannesson and Burdige, 2007; Arsouze et al., 2009). Lacan and Jeandel, 2005 underlined the potential of continental margins as a source for Nd and suggested that they might actually be the most important Nd source. They proposed an exchange of Nd at the ocean margins which modifies ϵ_{Nd} without considerably affecting $[Nd]_d$, and therefore introduced the term "boundary exchange". Another complementary source was suggested by Johannesson and Burdige, 2007, who estimate that a considerable fraction of Nd might enter the ocean through submarine ground water discharge. Finally, using different modelling approaches, Arsouze et al., 2007, Arsouze et al., 2009 have shown that a "boundary exchange" source is important to balance the oceanic Nd cycle. However, so far only little is known about the processes responsible for this boundary exchange.

This paper is organised as follows: First, we explain our approach for the simulation of Nd-isotopes ^{143}Nd and ^{144}Nd (Section 2). In Section 3 we explore the parameter space of two major tuning parameters of the Nd module, and derive a parametrisation for CTRL (i.e., the reference simulation) from these experiments. Simulated $[Nd]_d$ and ϵ_{Nd} are compared with observations, and the sensitivity of $[Nd]_d$ and ϵ_{Nd} to changes in the two major tuning parameters is discussed in detail. Furthermore, we show results from an experiment where we consider continental margins as unique source of Nd, and, in additional sensitivity experiments, examine the effect of changes in model parameters (i.e., diapycnal diffusion, and the Atlantic-to-Pacific freshwater flux) on $[Nd]_d$ and ϵ_{Nd}. Finally, in Section 4 we summarise our findings and discuss potential implications regarding the nature and magnitude of sources and sinks of Nd.

2. METHODS

2.1. The physical ocean model

The Bern3D model is based on a three-dimensional, frictional-geostrophic balance ocean model, developed by Edwards and Marsh, 2005, and Müller et al., 2006 who implemented a vertical resolution of 32 layers and an implicit scheme for the calculation of vertical transport. In its current set up the Bern3D model has a resolution of 36×36 cells and 32 depth layers in the vertical. In the horizontal, grid cells are equidistant in longitude and in the sine of latitude. Spacing in the vertical is logarithmic, ranging from 39 m at the surface to 397 m in the bottom layer. Under restoring boundary conditions, the model is forced by monthly climatologies of sea surface temperature (SST) and sea surface salinity (SSS) (Levitus and Boyer, 1994; Levitus et al., 1994), as well as wind stress (Kalnay et al., 1996).

In addition to prescribing SSS (under restoring boundary conditions), the model also allows the prescription of freshwater fluxes (mixed boundary conditions), or may be coupled to an energy balance model (Ritz et al., 2011). Mixed boundary conditions, which we are using in this study, require long-term averaged salinity fluxes to be diagnosed at the end of the spin-up phase, and to be kept fixed afterwards, thus enabling the development of circulation-salinity feedbacks and the perturbation of the model state. Since the publication of the paper of Müller et al., 2006 the topography has been updated to ETOPO5, and advective transport through the Bering Strait, as well as Indonesian throughflow have been included (Ritz et al., 2011).

The high computational efficiency makes the Bern3D model well suited for long-term paleoclimate simulations (Ritz et al., 2011; Tschumi et al., 2011) as well as extensive sensitivity studies (Tschumi et al., 2008,2010; Parekh et al., 2008; Müller et al., 2008; Gangstø et al., 2011) and permits the simulation of a high number of tracers in a consistent dynamical setting at the same time.

2.2. The biogeochemical model component

The biogeochemical model component applied in this study is described in detail elsewhere (Parekh et al., 2008; Tschumi et al., 2008). Export production of particulate organic carbon (POC), opal, and calcite ($CaCO_3$) is computed from prognostic equations. New production of POC and dissolved organic carbon are functions of light, iron (Fe), phosphate (PO_4^{-3}) and temperature and follow the parametrisation of Doney et al., 2006. Production of opal and $CaCO_3$ depends on new production as well as on the availability of silicic acid (Maier-Reimer et al., 2005). The depth of the euphotic zone, z_{eu}, is set to 75 m throughout the ocean according to the OCMIP-protocol.

Particles leaving the euphotic zone are instantaneously remineralised in the water column beneath following globally uniform, fixed remineralisation profiles. The downward fluxes of POC, F_{POC}, are prescribed by the power-law profile of Martin et al., 1987:

$$F_{POC}(z) = F_{POC}(z_{eu}) \cdot \left(\frac{z}{z_{eu}}\right)^{-\alpha} \quad \text{for } z > z_{eu}, \tag{2}$$

where z is the depth, z_{eu} is the depth of the euphotic zone, and α is a dimensionless coefficient (for more details see Table 1). The downward fluxes of opal and $CaCO_3$, F_{opal} and F_{CaCO_3}, are parametrised by exponential profiles with particle-specific dissolution length scales l_{opal} and $l_{calcite}$, according to

$$F_{opal}(z) = F_{opal}(z_{eu}) \cdot \exp\left(-\frac{z - z_{eu}}{l_{opal}}\right), \quad \text{for } z > z_{eu}, \tag{3a}$$

$$F_{CaCO_3}(z) = F_{CaCO_3}(z_{eu}) \cdot \exp\left(-\frac{z - z_{eu}}{l_{CaCO_3}}\right), \quad \text{for } z > z_{eu}, \tag{3b}$$

with $l_{opal} = 10$ km and $l_{calcite} = 3.5$ km. The remaining particle flux at the sea floor is instantaneously remineralised in the

Table 1
List of parameters, corresponding abbreviations, and their values as used in the text.

Variable	Symbol	CTRL	Unit
Total Nd concentration	$[Nd]_t$		pmol kg^{-1}
Dissolved Nd	$[Nd]_d$		pmol kg^{-1}
Particle-associated Nd	$[Nd]_p$		pmol kg^{-1}
Nd source, total	f_{tot}	6.1×10^9	g Nd yr^{-1}
Nd source density	$S_{tot}(\theta,\phi,z)$		g Nd m^{-3} yr^{-1}
Dust source, total	f_{du}	2.6×10^8	g Nd yr^{-1}
Dust source density	$S_{du}(\theta,\phi)$		g Nd m^{-3} yr^{-1}
Flux of dust	$F_{du}(\theta,\phi)$		g m^{-2} yr^{-1}
Nd-concentration dust	$c_{du,\,Nd}$	20	μg g^{-1}
Nd-release from dust	$\beta_{du,\,Nd}$	0.02	
Riverine source, total	f_{ri}	3.4×10^8	g Nd yr^{-1}
Riverine source density	$S_{ri}(\theta,\phi)$		g Nd m^{-3} yr^{-1}
River discharge	$F_{ri}(\theta,\phi)$		m^3 yr^{-1}
Nd-concentration, river	$c_{ri,\,Nd}(\theta,\phi)$		g Nd m^{-3}
Nd-removal, estuaries	$\gamma_{ri,\,Nd}$	0.7	
Boundary source, total	f_{bs}	5.5×10^9	g Nd yr^{-1}
Boundary source density	$S_{bs}(\theta,\phi,z)$		g Nd m^{-3} yr^{-1}
Total sediment surface	A_{tot}		m^2
Box sediment surface	$A(\theta,\phi,z)$		m^2
Box volume	$V(\theta,\phi,z)$		m^3
Thickness of euphotic layer	z_{eu}	75	m
Penetration depth of opal	l_{opal}	10000	m
Penetration depth of $CaCO_3$	$l_{calcite}$	3500	m
Dissolution constant of POC	α	0.9	
Particle settling velocity	v	1000	m yr^{-1}
Ratio $[Nd]_p$ to $[Nd]_d$	$[Nd]_p/[Nd]_d$	0.001	
Global average density of seawater	ρ	1024.5	kg m^{-3}
Diapycnal diffusivity	κ_D	10^{-5}	m^2 s^{-1}
Atlantic-to-Pacific freshwater flux	$Fw_{Atl-Pac}$	0.15	Sv

lowermost box of the model. Annually averaged export fields of opal and $CaCO_3$ are displayed in Fig. 1e and f. Patterns of particle fluxes fit observed large-scale patterns (Figs. 9.2.2, and 7.2.5b, Sarmiento and Gruber, 2006, respectively), and total annual export fluxes of POC (≈10 Gt Cyr^{-1}), $CaCO_3$ (≈0.9 Gt Cyr^{-1}), and opal (≈90 Tmol Si yr^{-1}) are comparable to available estimates (references in Sarmiento and Gruber, 2006; Tschumi et al., 2008).

Note, that the PISCES model which was used by Arsouze et al., 2009 is a more comprehensive biogeochemical model. It allows the simulation of big and small particles, which settle down the water column with different settling velocities. Furthermore, remineralisation of particles with depth is treated in a more process-based manner (see auxillary material to Aumont and Bopp, 2006). However, it also requires much more computational resources than the simpler biogeochemical model used in this study. The complexity of our biogeochemical module is consistent with the intermediate complexity of the Bern3D model and is well suited to the large number of simulations required for this study.

2.3. The neodymium model component, sources and sinks

In our model, we consider three different sources of Nd to the ocean: rivers, aeolian dust and the continental margins. Throughout the paper Nd refers to the sum of ^{143}Nd and ^{144}Nd

$$\mathrm{Nd} = {}^{143}\mathrm{Nd} + {}^{144}\mathrm{Nd}. \tag{4}$$

By rearranging and using the isotopic ratio, $IR = {}^{143}\mathrm{Nd}/{}^{144}\mathrm{Nd}$, we obtain the individual isotopic concentrations as follows:

$${}^{143}\mathrm{Nd} = \frac{\mathrm{Nd}}{(1/IR + 1)}, \tag{5a}$$

$${}^{144}\mathrm{Nd} = \frac{\mathrm{Nd}}{IR + 1}. \tag{5b}$$

Eqs. (5a) and (5b) are used to determine fluxes of ^{143}Nd and ^{144}Nd from information of fluxes of Nd and the associated isotopic ratio *IR*. Note, however, that neodymium has 7 stable isotopes with mass numbers 142, 143, 144, 145, 146, 148, and 150 of which ^{143}Nd and ^{144}Nd together account for only 36% (Magill et al., 2006). Therefore, to obtain fluxes of ^{143}Nd and ^{144}Nd from observed *total* Nd fluxes one would need to scale *total* Nd fluxes by 0.36. Conversely, in order to compare Nd of Eq. (4) with observed *total* Nd one would have to scale Nd by 1/0.36. Because of the constancy of this factor, we can simply use unscaled fluxes, i.e., *total* Nd fluxes are used in the model, and therefore the sum of the simulated ^{143}Nd and ^{144}Nd, i.e., Nd of Eq. (4), can be directly compared to observed *total* Nd.

Rivers and aeolian dust are the classical transport media of Nd to the oceans. In the model, Nd from rivers and dust enters the ocean in the uppermost layer only. Sediments on continental margins act as a source of a number of elements to the ocean (Lacan and Jeandel, 2005), and have recently been suggested to be the major source of Nd (Tachikawa

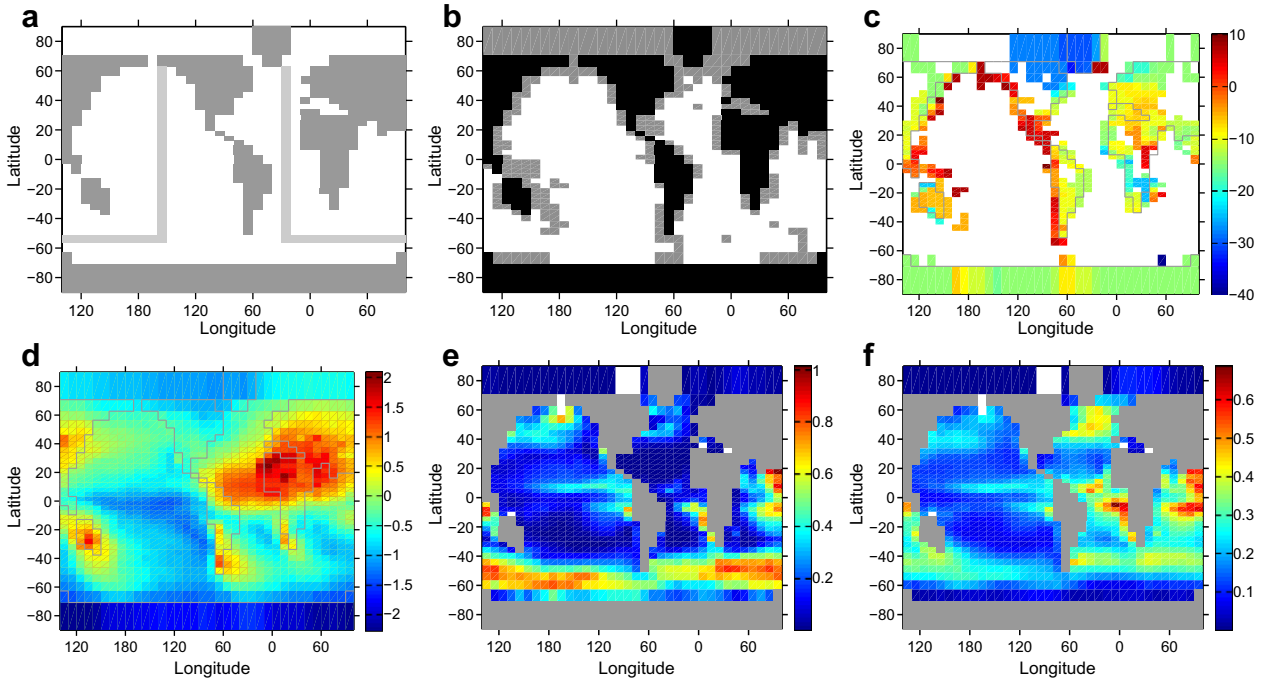

Fig. 1. (a) Global map and track of vertical sections shown in Figs. 5, 11, 12, 13, 14, and 16. (b) Global map indicating the continental margin in the Bern3D model (grid cells where seafloor is shallower than 3 km). (c) Global map of ϵ_{Nd} at continental margins, providing ϵ_{Nd} of the boundary source (following Jeandel et al., 2007). (d) Log10 values of yearly average atmospheric dust flux (g m^{-2} yr^{-1}, Luo et al., 2003). Steady-state export production of (e) opal (mol Si m^{-2} yr^{-1}) and (f) $CaCO_3$, (mol C m^{-2} yr^{-1}). Export production is calculated from prognostic equations (see Auxilliary Material of Tschumi et al., 2008, for a description). Annual mean export productions of about 92.9 Tmol Si yr^{-1} for opal, and about 1.0 Gt C yr^{-1} for $CaCO_3$ are comparable to estimates in Sarmiento and Gruber, 2006.

et al., 1999,Tachikawa et al., 2003; Lacan and Jeandel, 2005). Besides, due to the sedimentation of particles on the margins, these sediments also act as a sink of Nd. The exchange of Nd between sediment and the water column was denoted as boundary exchange. Nevertheless, this term, is not precise as it includes a large range of processes such as for example particle–seawater interactions (Lacan and Jeandel, 2005), and submarine groundwater discharge (Johannesson and Burdige, 2007). In our model, a boundary source is applied at the continental margins (i.e., sediments at depths between 0 and 3000 m). However, the continental margins also represent a boundary sink if settling particles reach the sediments in this place. For instance, Arsouze et al., 2009 reported that 64% of the sink are located at the continental margins. The combination of these two mechanisms accordingly represents the boundary exchange.

2.3.1. Dust source

Dust fluxes, $F_{du}(\theta,\phi)$, shown in Fig. 1d, are prescribed using the output of an atmospheric transport model (Luo et al., 2003). The Nd source per unit volume, $S_{du}(\theta,\phi)$, from dust is applied only in the surface ocean layer of the model. It is obtained by assuming a global mean concentration of Nd in dust, $c_{du,Nd}$ (Goldstein et al., 1984; Grousset et al., 1988,Grousset et al., 1998), of which a certain fraction $\beta_{du,Nd}$ (Greaves et al., 1994) is released (Table 1):

$$S_{du}(\theta,\phi) = F_{du}(\theta,\phi)\cdot c_{du,Nd}\cdot \beta_{du,Nd}\cdot \frac{1}{\Delta z_1}, \qquad (6)$$

where Δz_1 corresponds to the thickness of the uppermost ocean layer. The total dust-associated source (f_{du}) of Nd is about 2.6×10^8 g Nd yr^{-1}.

The dust source for individual Nd-isotopes is computed from prescribed isotopic ratios following Eqs. (5a) and (5b). Following Tachikawa et al., 2003, five different ocean regions are distinguished: North Atlantic, >50 °N, $\epsilon_{Nd}=-15$; Atlantic ⩽50 °N, $\epsilon_{Nd}=-12$; North Pacific >44 °N, $\epsilon_{Nd}=-5$; Indopacific ⩽44 °N, $\epsilon_{Nd}=-7$; Remainder, $\epsilon_{Nd}=-8$.

2.3.2. Riverine source

River discharge, $F_{ri}(\theta,\phi)$, and the Nd concentration, $c_{ri,Nd}(\theta,\phi)$, and isotopic composition, in river waters are prescribed following Goldstein and Jacobsen, 1987. The amount of Nd entering the pelagic ocean depends on the fraction, $\gamma_{ri,Nd}$, of dissolved Nd which is removed in estuaries (Goldstein and Jacobsen, 1987; Elderfield et al., 1990). Processes involved in this removal in estuaries are not well understood (e.g., Elderfield et al., 1990; Sholkovitz and Szymczak, 2000). Based on Goldstein and Jacobsen, 1987, and similar to previous modelling studies (Tachikawa et al., 2003; Arsouze et al., 2009), we assume, that 70% of Nd dissolved in rivers is removed in estuaries.

In analogy to Eq. (6), for the riverine Nd source per unit volume we write

$$S_{ri}(\theta,\phi) = F_{ri}(\theta,\phi)\cdot c_{ri,Nd}(\theta,\phi)\cdot(1-\gamma_{ri,Nd})\cdot\frac{1}{V_{\theta,\phi}}, \qquad (7)$$

where $F_{ri}(\theta,\phi)$ is the river discharge ($m^3\ yr^{-1}$), $c_{ri,Nd}(\theta,\phi)$ is the Nd concentration ($g\ Nd\ m^{-3}$), $\gamma_{ri,Nd}$ is the fraction which is removed in estuaries, and $V(\theta,\phi,z)$ is the volume of the grid cell with riverine input (m^3, see also Table 1). The global ocean source of Nd through river discharge is 3.4×10^8 g Nd yr^{-1}. This value is between the value reported by Goldstein and Jacobsen (1987; 5×10^8 g Nd yr^{-1}), and the value reported by Arsouze et al., 2009, 2.6×10^8 g Nd yr^{-1}.

2.3.3. Boundary source

The third Nd source considered in this study is the flux of Nd across the continental margins, the boundary source, $S_{bs}(\theta,\phi,z)$. In contrast to Nd entering the model through riverine and atmospheric transport, the boundary source is not restricted to the surface layer of the ocean. A given amount of Nd enters each model grid cell which is adjacent to sediment and which is located at a depth shallower than 3000 m (Fig. 1b). Three thousand meters is assumed to represent the lower boundary of the continental margins (Arsouze et al., 2007). The boundary source per unit area is constant with depth and globally uniform. The amount of Nd entering a given grid cell, thus only depends on the surface area ($A(\theta,\phi,z)$), which is adjacent to sediment. Similar to dust, we need to impose a value of ϵ_{Nd} to the boundary source. For this purpose we use a global map of ϵ_{Nd} at the continental margins (Fig. 1c; Jeandel et al., 2007). We calculate the source of each isotope for each grid cell following Eqs. (5a) and (5b), as well as

$$S_{bs}(\theta,\phi,z) = \frac{A(\theta,\phi,z)}{A_{tot}} \cdot f_{bs} \cdot \frac{1}{V_{\theta,\phi,z}}. \quad (8)$$

Here A_{tot} corresponds to the total sediment surface of the continental margins (i.e., between 0 and 3000 m). $A(\theta,\phi,z)$ is the sediment surface, and $V(\theta,\phi,z)$ the volume of a grid cell at a given longitude(θ), latitude (ϕ), and depth (z). Integrating $S_{bs}(\theta,\phi,z)$ over the entire ocean volume again yields the total boundary-associated Nd-source, f_{bs} (Table 1), which was used as a tuning parameter.

Note, in contrast to Arsouze et al., 2009, we do not take into account the Nd-concentration in sediments at the continental margins for the calculation of $S_{bs}(\theta,\phi,z)$, nor do we scale $S_{bs}(\theta,\phi,z)$ with depth. Therefore, apart from its depth range (0–3000 m), we do not make any assumption regarding the nature of the Nd boundary source. We do not assume spatial variations, but apply a flux of Nd to each square-meter of sediment which is constant in the vertical and in the horizontal direction.

2.3.4. Internal cycling – reversible scavenging

The only sink of Nd in our model is the removal of Nd from the water column by sinking particles. While particles reaching the seafloor are redissolved in the lowermost box of the water column, Nd associated to these particles is removed from the model. This sink balances the input of Nd by dust deposition, river inflow, and from continental margins.

We parametrise this sink by means of a reversible scavenging approach. This approach has already been used in various previous studies dealing with the ratio of protactinium and thorium (Pa/Th, Henderson et al., 1999; Marchal et al., 2000; Siddall et al., 2005,Siddall et al., 2007), Rare Earth Elements, REE, in general (e.g., Oka et al., 2009), and Nd isotopes in particular (Bertram and Elderfield, 1993; Siddall et al., 2008; Arsouze et al., 2009).

Reversible scavenging describes the physical process of adsorption and desorption of Nd on particle surfaces. The equilibrium between dissolved concentration, $[Nd]_d^j$, and concentration associated to particle-type i, $[Nd]_{p,i}^j$ (where i = POC, $CaCO_3$, opal), of each Nd isotope j, is described by a so-called "equilibrium scavenging coefficient":

$$K_i^j = \frac{[Nd]_{p,i}^j}{[Nd]_d^j \cdot R_i}, \quad (9)$$

where R_i is the dimensionless ratio of global average particle mass per cubic meter of seawater (C_i, Table 2) to the global average density ρ of seawater (1024.5 kg m^{-3}, Table 1) for each particle type i. The particle concentration for each particle-type i and each model grid cell, C_i', is calculated from the particle fluxes (Eqs. (2), (3a), and (3b)) by assuming a globally uniform settling velocity (1000 m yr^{-1}, Table 1), v, i.e., $C_i' = F_i/v$. A settling velocity of this magnitude is within the range of values applied for example in the PISCES model (Aumont and Bopp, 2006) and the same as was used by Siddall et al., 2005. The assumption of equilibrium between dissolved and particulate phase in the ocean is justified if adsorption and desorption are fast enough which was reported to be a reasonable assumption in the open ocean, e.g., for thorium (Henderson et al., 1999). As little is known about the partitioning of Nd between particulate and dissolved phases, we adopt this assumption for isotopes of Nd (similar to Siddall et al., 2008; Arsouze et al., 2009).

Both isotopes ^{143}Nd and ^{144}Nd are transported individually and independently in our model. Due to similar masses of ^{143}Nd and ^{144}Nd and because both are isotopes of the same element, isotopic fractionation during adsorption and desorption can be neglected, i.e., $[Nd]_p/[Nd]_d$ (and thus also K-values) is the same for ^{143}Nd and ^{144}Nd. So far only sparse information is available about particle-specific partitioning of dissolved and particle-associated concentration (i.e., preferential scavenging, Jeandel et al., 1995; Tachikawa et al., 1999; Siddall et al., 2008). We therefore avoid further complication arising from taking into ac-

Table 2
Global average particle concentrations of different particle types, used for the calculation of equilibrium scavenging coefficients following Eq. (9): particulate organic carbon (POC), opal, calcite ($CaCO_3$), and dust. Export fluxes of POC, opal, and $CaCO_3$ are calculated by the model, atmospheric dust fluxes are taken from Luo et al., 2003 and prescribed at the sea surface.

Particle type	Symbol	Value	Unit
POC	C_{POC}	2.3×10^{-6}	kg m^{-3}
$CaCO_3$	C_{CaCO_3}	1.1×10^{-6}	kg m^{-3}
Opal	C_{opal}	3.3×10^{-6}	kg m^{-3}
Dust	C_{dust}	1.3×10^{-6}	kg m^{-3}

count preferential scavenging and apply the same ratio $[Nd]_p/[Nd]_d$ to all particle types.

Adsorption onto particle surfaces takes place in areas where particles are present. Particles, and thus particle-associated Nd, are settling down the water-column due to gravitational force. Below the euphotic zone particles are becoming dissolved with increasing depth, and Nd adsorbed onto particle surfaces is released back to seawater (i.e., desorbed).

Particles therefore act as ocean internal sinks for dissolved Nd at shallow depths and as sources at greater depths. In the model this combined internal source and sink is described by the following equation:

$$S^j(rs) = \frac{\partial(v \cdot [Nd]_p^j)}{\partial z}, \tag{10}$$

where v is the globally uniform settling velocity of particles (1000 m yr^{-1}, Table 1), $[Nd]_p^j$ is the total particle-associated concentration. Release of $[Nd]_p^j$ from particles at depths below the euphotic zone causes $[Nd]_d$ to increase with increasing depth, and increasing age of the water mass. A similar pattern is observed, e.g., for Si, and PO_4^{-3}, which lead to the term of "nutrient-like" behavior (Goldstein and Hemming, 2003).

For each grid cell and each isotope we sum up sources from dust ($S_{du}(\theta,\phi)$, Eq. (6)), rivers ($S_{ri}(\theta,\phi)$, Eq. (7)), and the continental margin ($S_{bs}(\theta,\phi,z)$, Eq. (8)) into one single term $S_{tot}(\theta,\phi,z)$. After adding the source provided by reversible scavenging (Eq. (10)) the conservation equations for ^{143}Nd and ^{144}Nd write as follows:

$$\frac{\partial [Nd]_t^j}{\partial t} = S_{tot}([Nd]_d^j) - \frac{\partial(v \cdot [Nd]_p^j)}{\partial z} + T([Nd]_t^j), \tag{11}$$

where $[Nd]_t^j$ indicates the total concentration of isotope j, and T corresponds to the physical transport (advection, convection, diffusion) provided by the Bern3D model.

Eq. (11) illustrates that, instead of transporting both $[Nd]_d^j$ and $[Nd]_p^j$ of each isotope, the model transports the total concentration $[Nd]_t^j$, which is made up of dissolved and particulate concentration:

$$[Nd]_t^j = [Nd]_p^j + [Nd]_d^j. \tag{12}$$

For each particle type we rearrange and insert Eq. (9) into Eq. (12),

$$[Nd]_t^j = R_{POC} \cdot K_{POC} \cdot [Nd]_d^j + R_{CaCO_3} \cdot K_{CaCO_3} \cdot [Nd]_d^j + R_{opal} \cdot K_{opal} \cdot [Nd]_d^j + R_{dust} \cdot K_{dust} \cdot [Nd]_d^j + [Nd]_d^j, \tag{13}$$

which leads to

$$[Nd]_d^j = \frac{[Nd]_t^j}{1 + \sum_{i=1}^{M} K_i^j \cdot R_i}, \tag{14}$$

where i denotes the corresponding particle type. Using Eqs. (14) and (12), $[Nd]_d^j$ and $[Nd]_p^j$ can be calculated a posteriori, thus making the Nd-model more cost-efficient (Siddall et al., 2005).

In contrast to our model, the model of Arsouze et al., 2009 simulates two different particle size classes, and applies different settling velocities to these size classes. Moreover, to obtain a better agreement between simulated and observed $[Nd]_d$ and ϵ_{Nd}, Arsouze et al., 2009 apply different $[Nd]_p/[Nd]_d$ to big and small particles, and thus introduce a differentiation into the reversible scavenging.

2.4. Cost function for model tuning

To evaluate the performance of each simulation, we minimised a cost function

$$J = \frac{1}{N} \sum_{k=1}^{N} |obs_k - sim_k|, \tag{15}$$

where obs_k and sim_k is either $[Nd]_d$ or ϵ_{Nd}, and k is an index over all observations. Thus we calculate J for $[Nd]_d$ and ϵ_{Nd}, i.e., $J_{[Nd]_d}$ and $J_{\epsilon_{Nd}}$, which define the mean deviation of simulated from observed values of $[Nd]_d$ and ϵ_{Nd} in pmol kg^{-1} and ϵ_{Nd}-units, respectively. If more than one observation is available within one model grid cell, the arithmetic mean is used for the calculation of $J_{[Nd]_d}$ and $J_{\epsilon_{Nd}}$.

Observations of $[Nd]_d$ and ϵ_{Nd}, used in this study, have been downloaded from the web (http://www.legos.obs-mip.fr/fr/equipes/geomar/results/database_may06.xls). See Jones et al., 2008 and Siddall et al., 2008 for a list of references. We completed this compilation by dissolved Nd concentrations from Elderfield and Greaves, 1982, Greaves et al., 1999, Andersson et al., 2008 and Porcelli et al., 2009. Note that the distribution of the observations is not homogeneous, neither in the horizontal coverage of the ocean nor in the vertical (not shown). This will bias $J_{[Nd]_d}$ and $J_{\epsilon_{Nd}}$ towards regions where most observations are available.

2.5. Overview of experiments

To find a combination of tuneable parameter values of the model which yields results most consistent with the observational evidence, we ran a large number of experiments within which we systematically varied the magnitude of the main source, f_{bs}, and the parametrisation of the reversible scavenging, i.e., $[Nd]_p/[Nd]_d$. The reversible scavenging coefficient K for each particle type is calculated based on the global mean concentration of the corresponding particle type and $[Nd]_p/[Nd]_d$ (Eq. (9)). Parameter values apart from f_{bs} and $[Nd]_p/[Nd]_d$ are kept constant. By minimising $J_{[Nd]_d}$ and $J_{\epsilon_{Nd}}$, we constrain the range of reasonable parameter values for both f_{bs} and $[Nd]_p/[Nd]_d$, and thus obtain a plausible parametrisation for CTRL. Based on CTRL, we examine the effect of variations in values of f_{bs} and $[Nd]_p/[Nd]_d$ on $[Nd]_d$ and ϵ_{Nd} in detail. For this purpose, we present results from experiments, where we doubled and halfed each of these values.

Tachikawa et al., 2003, as well as Arsouze et al., 2009, indicate that, by taking into account dust and river sources only, neither $[Nd]_d$ nor ϵ_{Nd} can be simulated within the range of observations. In contrast, in experiment DR00 we omit input from rivers and dust, leaving the continental margins as the only source (f_{bs} equals f_{tot}). Thus the importance of dust and river sources, as well as the potential of the boundary source to serve as single Nd-source are further explored.

The Bern3D model has been parametrised by comparing simulated and observed profiles of a number of transient tracers, and surface to deep ocean transport is simulated realistically (Müller et al., 2006). Values for κ_D and $Fw_{Atl-Pac}$ as published by Müller et al., 2006 are applied to the CTRL (1.0×10^{-5} m s^{-2} and 0.15 Sv, respectively). This results in a simulated annual mean Atlantic overturning circulation of about 16.2 Sv, consistent with estimates derived from hydrographic data (Ganachaud and Wunsch, 2000; Talley et al., 2003). However, some degree of uncertainty regarding the choice of these values remains. As in ocean circulation models both the strength and the geometry of the overturning circulation depend on κ_D and $Fw_{Atl-Pac}$, the values applied to these parameters probably affect the distribution of $[Nd]_d$ and ϵ_{Nd}. We assess the robustness of results obtained with the CTRL in additional experiments by applying different values to κ_D and $Fw_{Atl-Pac}$.

For each experiment, the model was run until steady-state was achieved (i.e., the inventory of Nd is constant), which depends on the mean residence time of Nd. Thus the length of the simulations ranges from 7 to 20 kyr. Results of the sensitivity experiments are then compared to the CTRL.

3. MODEL RESULTS

3.1. Exploring the parameter space of $[Nd]_p/[Nd]_d$, and f_{bs}

Fig. 2 shows values of $J_{[Nd]_d}$ and $J_{\epsilon_{Nd}}$ of 255 different simulations, where we systematically varied $[Nd]_p/[Nd]_d$, and f_{bs}. On the x-axis, $[Nd]_p/[Nd]_d$ ranges from 0.003 to 0.0017. On the y-axis, f_{bs} ranges from 0 to 11×10^9 g Nd yr^{-1}. $f_{bs} = 0$, corresponds to the case where dust and rivers are the only sources of Nd. This has already

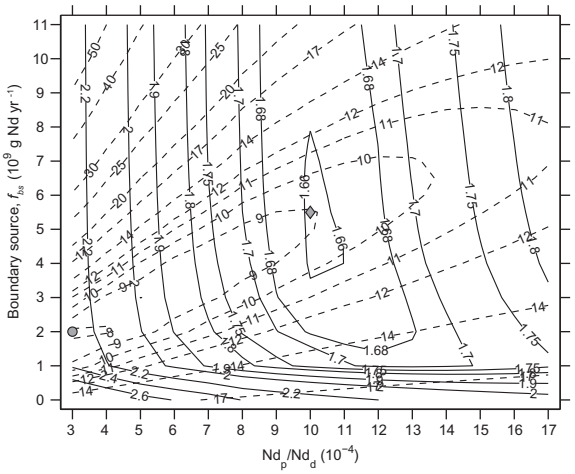

Fig. 2. Contours of cost functions $J_{[Nd]_d}$ (dashed) and $J_{\epsilon_{Nd}}$ (solid) indicating the global average deviations of simulated from observed $[Nd]_d$ and ϵ_{Nd}, for different parametrisations of the Nd module. $J_{[Nd]_d}$ and $J_{\epsilon_{Nd}}$ are calculated following Eq. (15). Units are pmol kg^{-1} and ϵ_{Nd}-units, respectively. Variations in $J_{[Nd]_d}$ and $J_{\epsilon_{Nd}}$ indicate the sensitivity of the model to different values of f_{bs} (y-axis) and $[Nd]_p/[Nd]_d$ (x-axis). Combinations of parameters of f_{bs} and $[Nd]_p/[Nd]_d$, for which $J_{[Nd]_d}$ and $J_{\epsilon_{Nd}}$ reach minima, are indicated by a filled circle and a diamond, respectively.

been discussed by Tachikawa et al., 2003 and Arsouze et al., 2009, and we are not investigating it in greater detail here. Note, however, the low consistency with observations as indicated by large values of $J_{[Nd]_d}$ and $J_{\epsilon_{Nd}}$. $f_{bs} = 11 \times 10^9$ g Nd yr^{-1} corresponds to the estimate of Arsouze et al., 2009.

In Fig. 2, $J_{[Nd]_d}$ is large in cases where $[Nd]_p/[Nd]_d$ is small and f_{bs} is large, or vice versa (indicated by dashed lines). In contrast, $J_{[Nd]_d}$ is small if both, $[Nd]_p/[Nd]_d$ and f_{bs} are small, reaching a minimum for $f_{bs} \approx 2 \times 10^9$ g Nd yr^{-1}, and $[Nd]_p/[Nd]_d \approx 3 \times 10^{-4}$ indicated by a filled circle. However, $J_{[Nd]_d}$ increases only slightly if $[Nd]_p/[Nd]_d$ and f_{bs} increase in tandem. In the setup where $J_{[Nd]_d}$ reaches a minimum, $[Nd]_d$ is simulated within the range of observations, and distributions of observed and simulated $[Nd]_d$ indicate reasonable agreement (Figs. 3a–d and 5a). Furthermore, the global Nd inventory (6.2×10^{12} g Nd) does not differ much from estimates of Tachikawa et al., 2003 and Arsouze et al., 2009 (4.2×10^{12} g Nd). Though, in this setup, the overall performance in simulating ϵ_{Nd} is relatively low (Fig. 2). For example the interbasin gradient of ϵ_{Nd} is not well pronounced (Figs. 4a and 5b). This can be explained by the large mean residence time ($\tau_{Nd} \approx 1700$ yr), which is about twice the estimated mean ocean mixing time of the model (≈830 yr, obtained with an ideal age tracer, e.g., Sarmiento et al., 1990), and thus prevents the build up of an interbasin gradient as observed in the modern ocean.

Compared to $J_{[Nd]_d}$, the pattern of $J_{\epsilon_{Nd}}$ is different. For low values of f_{bs} (range of f_{bs}: 0–11×10^{-9} g Nd yr^{-1}), $J_{\epsilon_{Nd}}$ decreases with increasing magnitude of f_{bs}, but does not change much for any further increase beyond $f_{bs} \approx 2 \times 10^9$ g Nd yr^{-1}. Instead, beyond this value, $J_{\epsilon_{Nd}}$ mainly changes with variations in $[Nd]_p/[Nd]_d$, and reaches a minimum for $f_{bs} \approx 5.5 \times 10^9$ g Nd yr^{-1}, and $[Nd]_p/[Nd]_d \approx 1 \times 10^{-3}$ indicated by a filled diamond in Fig. 2. For this setup, distributions of observed and simulated ϵ_{Nd} are in reasonable agreement, and simulated ϵ_{Nd} agree well with observations (Figs. 4e–h, and 5d). The Nd global inventory is similar to estimates of 4.2×10^{12} g Nd (Tachikawa et al., 2003; Arsouze et al., 2009), as is f_{bs} (8.1 and 11×10^9 g Nd yr^{-1}, respectively, see also Table 3). τ_{Nd} is about 700 yr, which is slightly lower than the mean ocean mixing time (about 830 yr, Table 3). The interbasin gradient of ϵ_{Nd} is thus well pronounced (Fig. 4e–h). The distribution of simulated $[Nd]_d$ roughly agrees with the distribution of observations, and $[Nd]_d$ is simulated within the observational range (Fig. 3). However, particularly in the North Atlantic $[Nd]_d$ is rather too low in depths shallower than 1000 m (Fig. 5).

Overall, the parameter study shows that it is not possible to find a combination of f_{bs} and $[Nd]_p/[Nd]_d$ which would produce minima in both, $J_{[Nd]_d}$ and $J_{\epsilon_{Nd}}$. Any reference choice, therefore, constitutes a compromise to some extent. For our CTRL, we apply values of 5.5×10^9 g Nd yr^{-1} and 0.001 for f_{bs} and $[Nd]_p/[Nd]_d$, respectively, which correspond to the set up where $J_{\epsilon_{Nd}}$ is smallest (indicated by a filled diamond in Fig. 2). Results obtained with this parametrisation are presented in more detail in the following section. However, we note that an evaluation of the model

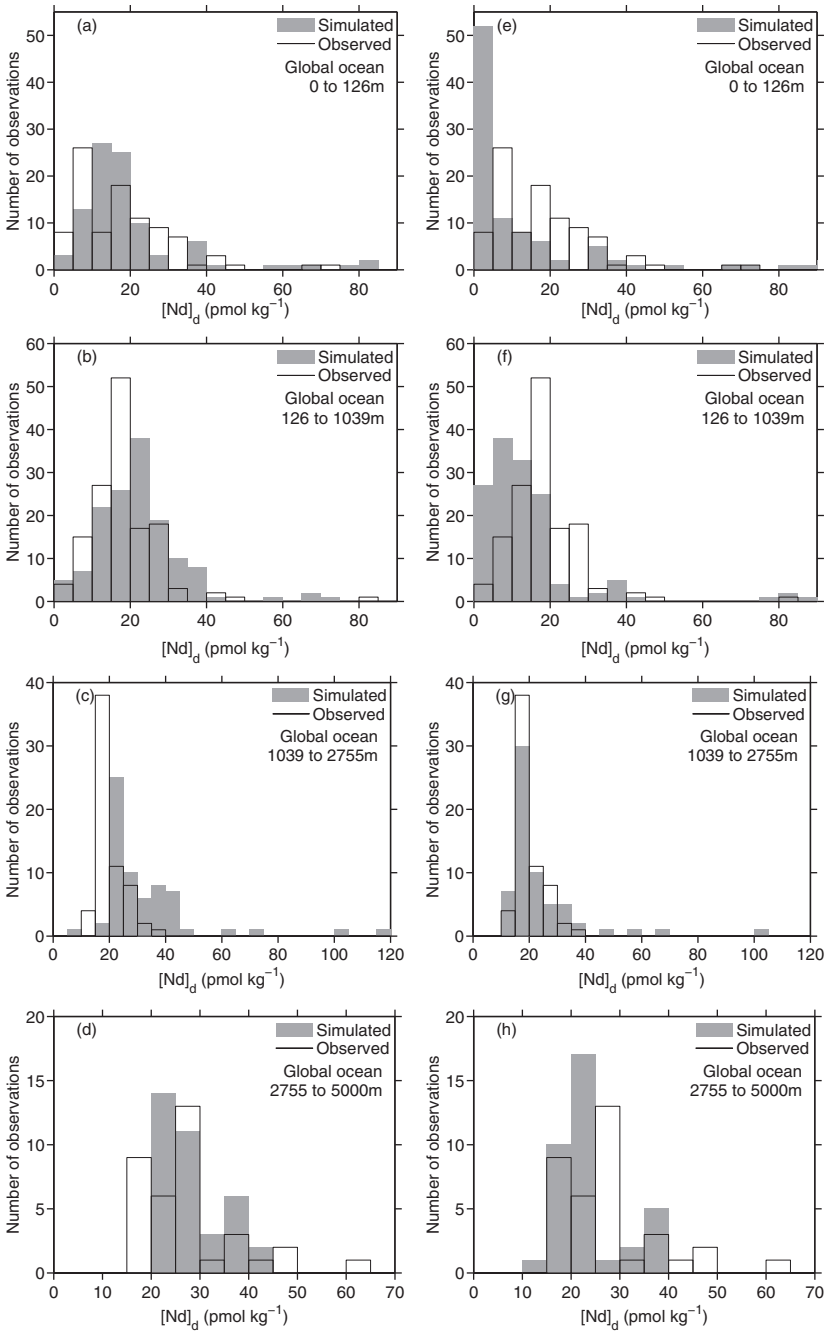

Fig. 3. Histograms showing the distribution of simulated (grey bins) and observed (open bins indicated by lines) $[Nd]_d$, for parametrisations where $J_{[Nd]_d}$ (a–d) and $J_{\epsilon_{Nd}}$ (e–h) produce minima (indicated by a filled circle and a filled diamond in Fig. 2). Shown are values from certain depth ranges (details on panels). Simulated values are from grid cells where observations are available. If more than one observation is available within one grid cell, the arithmetic mean is shown.

performance based on $J_{[Nd]_d}$ and $J_{\epsilon_{Nd}}$ alone, may be biased due to the limited amount of data available, particularly as these observations are not distributed homogeneously. Furthermore, our assumption of a globally uniform flux of f_{bs} probably is not valid (e.g., Haley et al., 2004). Apart from the low resolution of our model, particularly in high latitudes, our simplified approach may be one reason for the fact that the we cannot find a combination of f_{bs} and $[Nd]_p/[Nd]_d$ which produces minima in both, $J_{[Nd]_d}$ and $J_{\epsilon_{Nd}}$.

3.2. The CTRL

In the CTRL, f_{tot} sums up to 6.1×10^9 g Nd yr^{-1}. Ninety percent of f_{tot} are contributed by the boundary source (f_{bs}), 6% by rivers (f_{ri}) and 4% by airborne dust (f_{du}). About 70% and 83% of the observed values of $[Nd]_d$ and ϵ_{Nd}, are simulated within ± 10 pmol kg^{-1} and ± 3 ϵ_{Nd}-units, respectively (see Table 3 for more details).

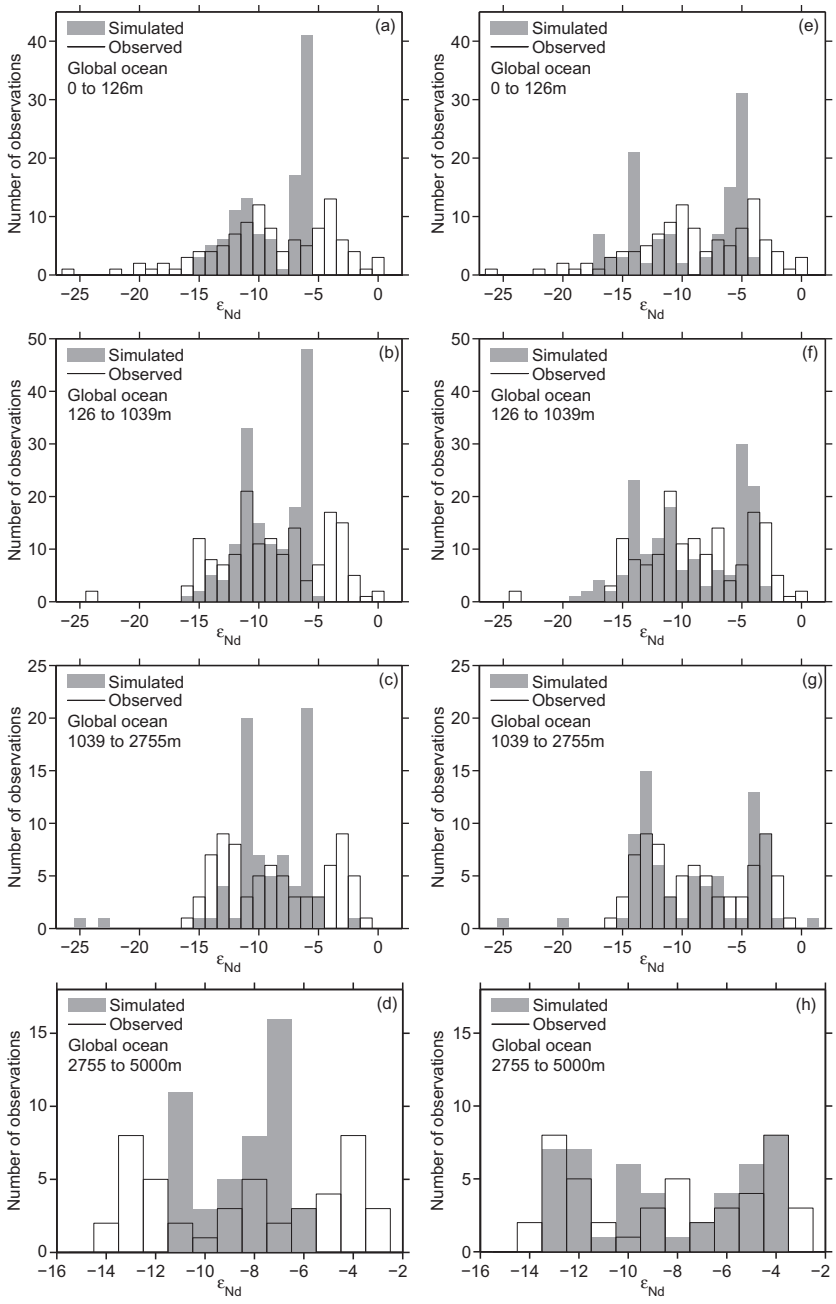

Fig. 4. Histograms showing the distribution of simulated (grey bins) and observed (open bins indicated by lines) ϵ_{Nd}, for parametrisations where $J_{[Nd]_d}$ (a–d) and $J_{\epsilon_{Nd}}$ (e–h) produce minima (indicated by a filled circle and a filled diamond, in Fig. 2). Shown are values from certain depth ranges (details on panels). Simulated values are from grid cells where observations are available. If more than one observation is available within one grid cell, the arithmetic mean is shown.

3.2.1. Distributions of observed and simulated $[Nd]_d$ and ϵ_{Nd}

Distributions of simulated and observed values of $[Nd]_d$ and ϵ_{Nd} from different depth ranges (0–126 m, >126–1039 m, >1039–2755 m, 2755–5000 m) globally, as well as from different basins (Atlantic, Pacific, Indian), are compared in Figs. 3a–d, and 6a–l, and in Figs. 4a–d and 7a–l, respectively.

Simulated $[Nd]_d$ is within the range of observations in individual basins as well as on a global scale (Figs. 3a–d and 6a–l). However, $[Nd]_d$ is rather too low in the Atlantic particularly at shallow depths (0–126 and >126–1039 m, Fig. 6a and b). Largest deviations are found in the Atlantic (more precisely in the North Atlantic and Arctic, not discernible in Fig. 6). ϵ_{Nd} at all depths, on a global scale, as well as in individual basins, is simulated in good agreement with observations. Nevertheless, the simulated range of ϵ_{Nd} is smaller than observed, i.e., largest and smallest observations are not simulated by the CTRL (Figs. 4a–d and 7a–l).

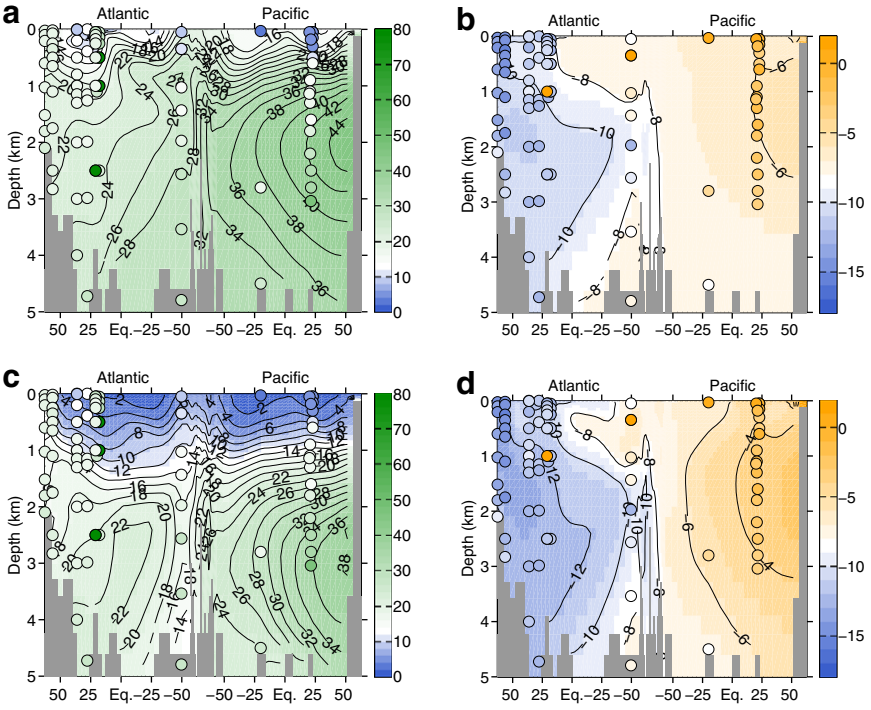

Fig. 5. Vertical sections of $[Nd]_d$ (left), and ϵ_{Nd} (right), along a track from the North Atlantic to the North Pacific, traversing the Southern Ocean from West to East (as indicated in Fig. 1a). Shown are results from parametrisations where $J_{[Nd]_d}$ (a and b) and $J_{\epsilon_{Nd}}$ (c and d) produce minima (indicated by a filled circle and a filled diamond, in Fig. 2). Simulated values in the Atlantic are from 20 to 30 °W, observations are from 10 to 40 °W. Simulated values in the Pacific are from 150 to 160 °W, and observations are from 140 to 170 °W. In the Southern Ocean, simulated values are from ≈51–56 °S. The length of the Southern Ocean passage is scaled with a factor of 1/10 in horizontal direction. Observations are superimposed as colored circles, using the same color scale.

Table 3
Set up of experiments. See also Table 1 for an explanation of abbreviations. $J_{[Nd]_d}$ and $J_{\epsilon_{Nd}}$ indicate global average deviations of simulated from observed $[Nd]_d$ and ϵ_{Nd}, respectively, and are calculated following Eq. 15. J_1 and J_2 indicate the percentage of observations of $[Nd]_d$ and ϵ_{Nd}, which are simulated within ±10 pmol kg^{-1}, and ±3 ϵ_{Nd}-units, respectively.

Experiment	$\frac{[Nd]_p}{[Nd]_d}$ (1)	f_{bs} g Nd yr^{-1}	I g Nd	τ_{Nd} yr	$J_{[Nd]_d}$ pmol kg^{-1}	$J_{\epsilon_{Nd}}$ ϵ_{Nd} (1)	J_1 %	J_2 %
CTRL	0.001	5.5×10^9	4.2×10^{12}	700	9	1.66	70	83
BS05	0.001	2.75×10^9	2.3×10^{12}	700	11	1.66	57	83
BS20	0.001	11.0×10^9	8.1×10^{12}	700	19	1.66	41	83
PD05	0.0005	5.5×10^9	7.7×10^{12}	1270	16	1.97	50	79
PD20	0.002	5.5×10^9	2.0×10^{12}	330	13	1.91	51	78
DR00	0.001	6.1×10^9	4.2×10^{12}	700	10	1.69	66	82

3.2.2. Sea floor maps

Figs. 8 and 9 show simulated $[Nd]_d$ and ϵ_{Nd} at the sea floor (i.e., within the lowermost box of each gridpoint). We included all observations which are available from a depth between the real sea floor depth and a depth of 500 m above the corresponding grid cell depth. Observed $[Nd]_d$ and ϵ_{Nd} are depicted as circles, colored using the same color scale as underlying model results. In Fig. 9, we also show ϵ_{Nd} measured on manganese crusts as colored diamonds (from the database of Frank, 2002). Manganese crusts integrate ϵ_{Nd} of surrounding waters over thousands of years (e.g., glacial interglacial time-scales), and therefore indicate a large-scale inter-basin gradient not only in recent observations, but also on longer time scales. Additional depth profiles in Fig. 9 illustrate the observed and simulated evolution of $[Nd]_d$ and ϵ_{Nd} with depth, and are discussed in Section 3.2.3.

The global map of simulated $[Nd]_d$ at the sea floor indicates low values in the North Atlantic (<20 pmol kg^{-1}) and high values in the North Pacific (>35 pmol kg^{-1}). Intermediate values are simulated in the Indian and the Southern Ocean (20–30 pmol kg^{-1}). In general, $[Nd]_d$ at the sea floor increases with increasing age of the water mass, i.e., along the circulation pathway. This pattern is in agreement with observations (Fig. 8). Fig. 9 indicates high (radiogenic) values of ϵ_{Nd} in the North Pacific, while ϵ_{Nd} is low (unradiogenic) in the North Atlantic. Lowest values of ϵ_{Nd} occur in the NW-Atlantic (i.e., Labrador Seas, $\epsilon_{Nd} < -20$), and highest values in the northernmost North Pacific ($\epsilon_{Nd} \approx 0$). In contrast, ϵ_{Nd} in the Indian and Southern Oceans is inter-

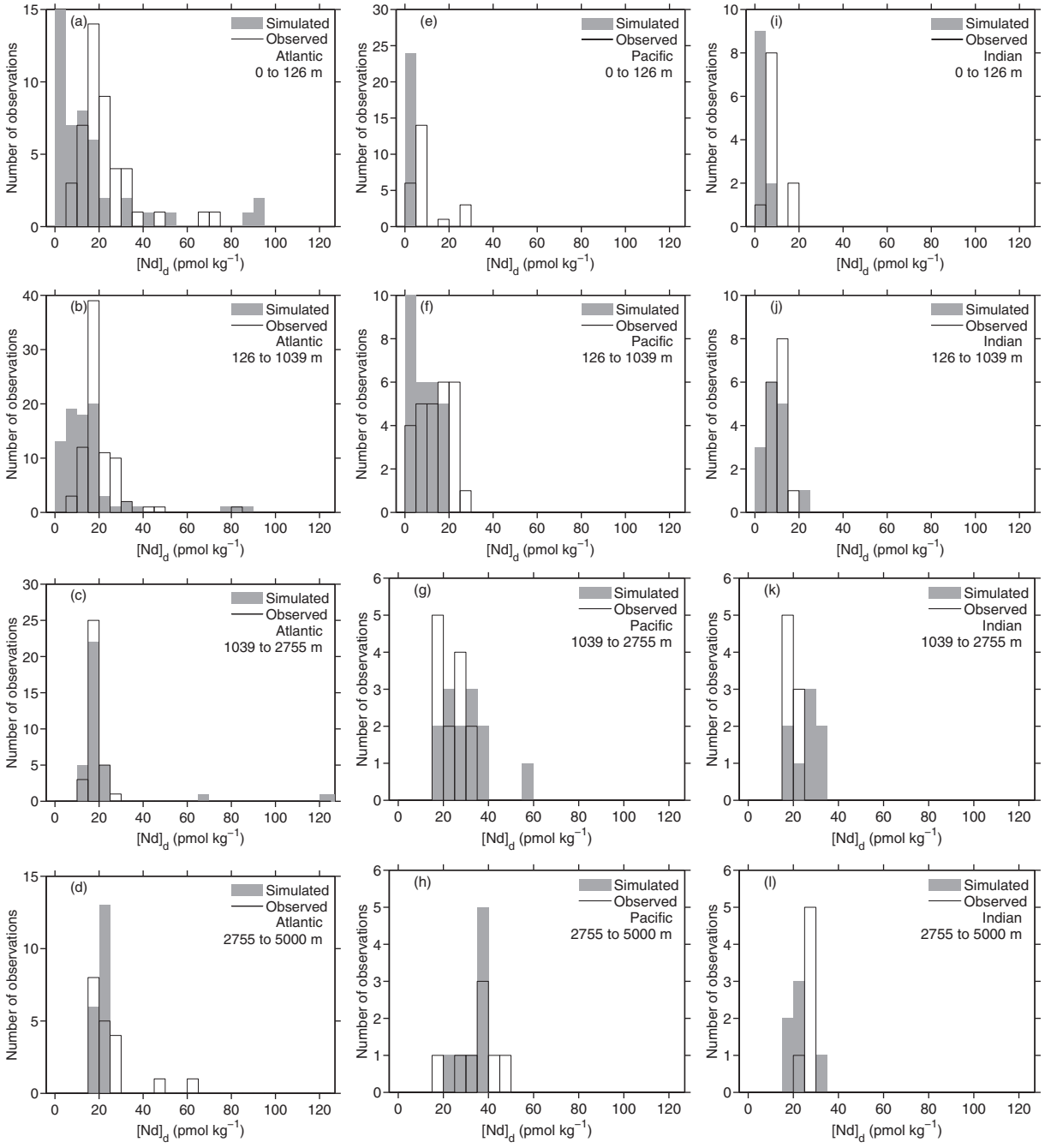

Fig. 6. Histograms showing the distribution of simulated (grey bins) and observed (open bins indicated by lines) $[Nd]_d$, obtained with CTRL. Shown are values from certain depth ranges (top to bottom) and from different basins (left to right, further details on panels). Simulated values are from grid cells where observations are available. If more than one observation is available within one grid cell, the arithmetic mean is shown.

mediate, simulated values are around −7 to −9. Despite some minor, spatially restricted, deviations from observations, e.g., in the Northeast Atlantic, the simulated pattern is consistent with available observations.

3.2.3. Profiles and cross-sections

In Fig. 5c and d, we show Atlantic-to-Pacific cross-sections of $[Nd]_d$ and ϵ_{Nd}, traversing the Southern Ocean in an eastward direction. The track of the cross-section is indicated in Fig. 1a. Simulated values are from 20 to 30 °W in the Atlantic basin, from 150 to 160 °W in the Pacific, and from ≈54 to 56 °S in the Southern Ocean. Observations are superimposed as colored circles using the same color scale. In the Atlantic, observations are located between 10 and 40 °W and between 140 and 170 °W in the Pacific. Apart from profile #5 in Figs. 8 and 9, which is located

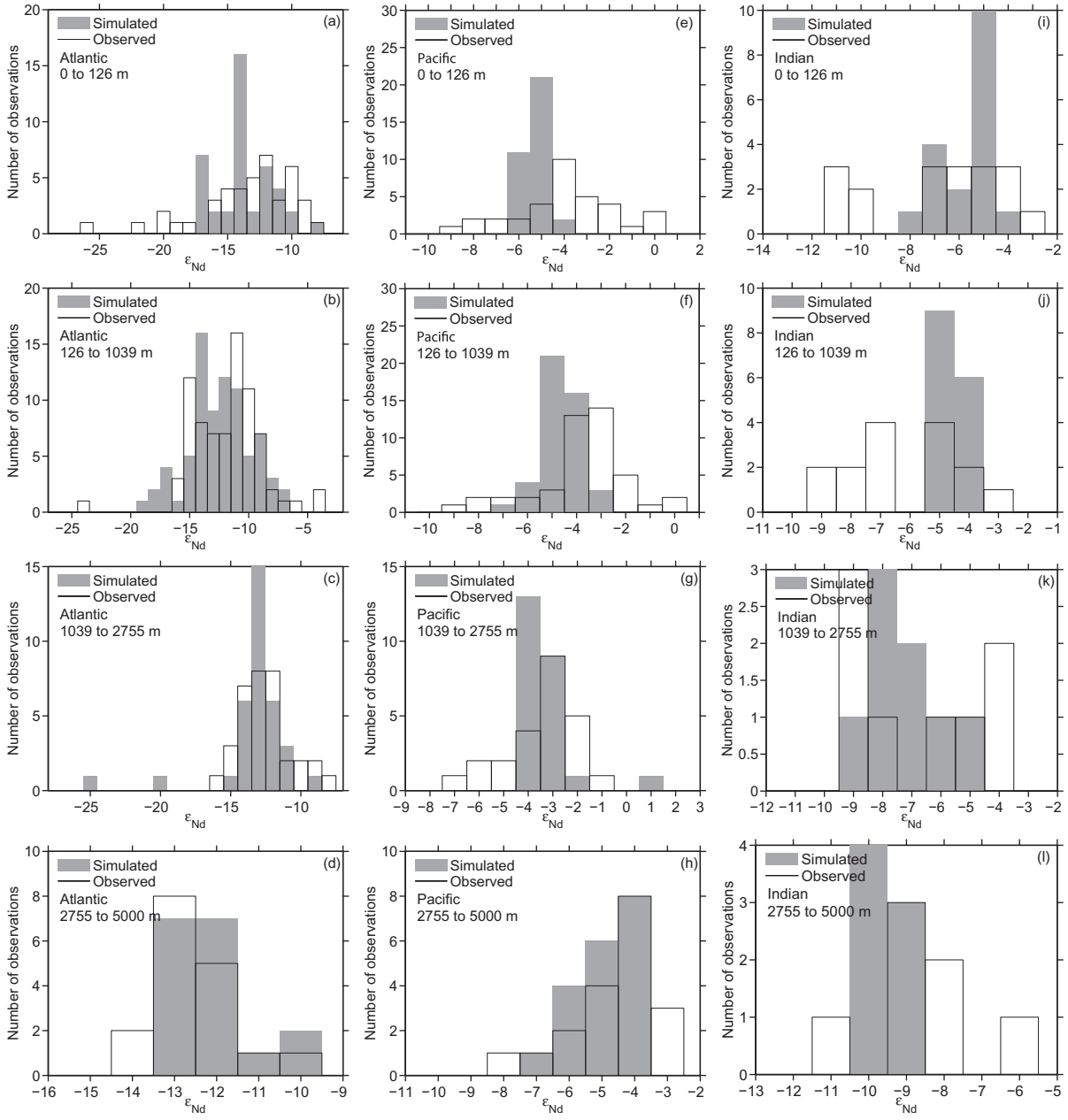

Fig. 7. Histograms showing the distribution of simulated (grey bins) and observed (open bins indicated by lines) ϵ_{Nd}, obtained with CTRL. Shown are values from certain depth ranges (top to bottom) and from different basins (left to right, further details on panels). Simulated values are from grid cells where observations are available. If more than one observation is available within one grid cell, the arithmetic mean is shown.

in the southern Atlantic, no observations are available along the track through the Southern Ocean. We also discuss profiles of $[Nd]_d$ and ϵ_{Nd} from different locations (Figs. 8 and 9, profiles #1–8).

In Fig. 8 we have shown, that $[Nd]_d$ increases from the Atlantic to the Pacific Ocean in the lowermost boxes. This increase also becomes obvious in the cross-section (Fig. 5c). $[Nd]_d$ increases from $\approx$10 pmol kg^{-1} in the upper layers of the North Atlantic to $\approx$20 pmol kg^{-1} in the deep South Atlantic. In the Southern Ocean, $[Nd]_d$ slightly increases from east to west (from $\approx$17 to 24 pmol kg^{-1}), and in the Pacific region, $[Nd]_d$ is $\approx$24 pmol kg^{-1} in deep waters of the Southern Hemisphere and reaches values $>$40 pmol kg^{-1} in the North Pacific. In addition to an increase along the circulation pathway, $[Nd]_d$ also increases with depth. With $[Nd]_d$ as low as $\approx$2 pmol kg^{-1}, surface waters are almost depleted of $[Nd]_d$ in the Atlantic as well as in the Pacific. However, $[Nd]_d$ is not depleted at all latitudes. $[Nd]_d$ is particularly low in surface waters in the tropics and subtropics, but higher at high latitudes, reaching values of $\approx$12 pmol kg^{-1} in the North Atlantic. Furthermore, particularly in some boxes in the North Atlantic,

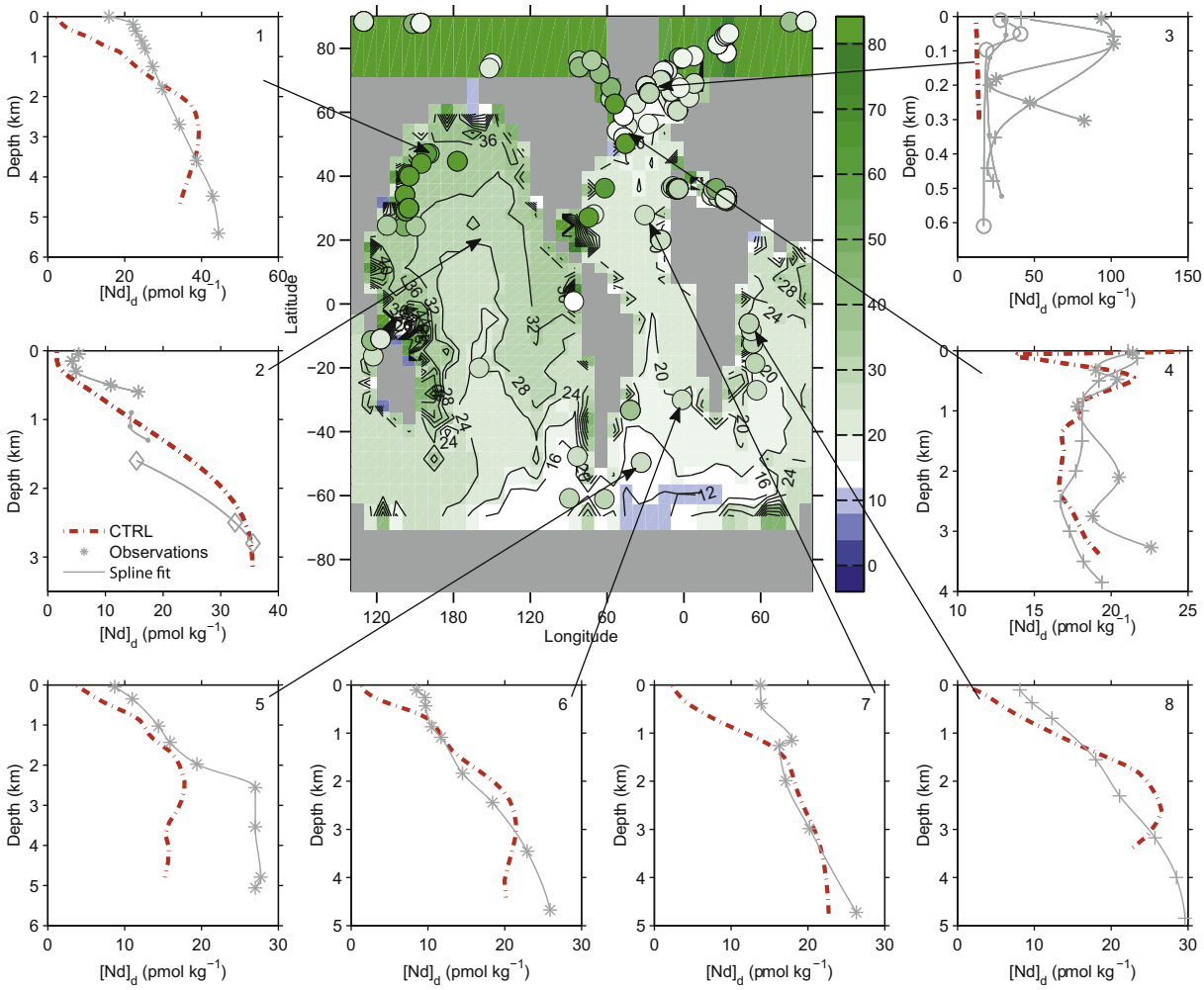

Fig. 8. Global map of $[Nd]_d$ at the sea floor (i.e., in the lowermost box of the model, central panel), obtained with CTRL. Observations between the seafloor and 500 m above the depth of the corresponding grid cell are superimposed using the same color coding. Profiles in adjacent panels show observed and simulated values of $[Nd]_d$. Different markers indicate different observations. Observations were fitted using a cubic spline, arrows indicate the approximate location of each profile.

$[Nd]_d$ does not increase at all, but is constant throughout the water column. Such a pattern is due to convective activity in regions of deep water formation, which prevents the build up of a vertical gradient within the water column. Rather uniform $[Nd]_d$ within the water column can also be identified in some of the observed profiles of this area (e.g., Fig. 8, profile #3).

We have shown that $[Nd]_d$ at the sea floor matches observations in sea water quite well (Fig. 8). From the cross-section it becomes clear that this is true not only for the seafloor but for most of the deep water masses in the Atlantic and the Pacific (Fig. 5c). In contrast, simulated $[Nd]_d$ deviates from observed $[Nd]_d$ in surface and intermediate depths of the Atlantic, and particularly the Arctic Ocean (Fig. 6a). E.g., $[Nd]_d$ is too low in North Atlantic surface layers, and below the Saharan dust-plume. Furthermore, compared to observations, in the Atlantic section of the Southern Ocean the increase of $[Nd]_d$ with depth is too small (profile #5 in Fig. 8). Note, that simulated $[Nd]_d$ particularly in the Arctic Ocean suffer from the low resolution of the model. Nevertheless, in additional experiments we found that high $[Nd]_d$ in the Arctic hardly affect $[Nd]_d$ or ϵ_{Nd} outside this basin (not shown). Simulated ϵ_{Nd} of main water masses in the Atlantic as well as in the Pacific, matches observed values. ϵ_{Nd} is around -13.5 in NADW, and -7 to -9 in AAIW and AABW, respectively, laying well within the range of observations (Figs. 5d, and 9, profiles #4–7). As ϵ_{Nd} considerably varies with water mass, observed depth profiles which sample different water masses show a so-called "zig-zag"-pattern, i.e., strongly varying ϵ_{Nd}-values, within a single profile (Goldstein and Hemming, 2003). CTRL reasonably simulates the "zig-zag"-structure of such profiles (Figs. 5d, and 9, profiles #5–7). However, ϵ_{Nd} is slightly underestimated in the tongue of NADW in the South Atlantic (profile #5, Fig. 9). Deviations from observations can also be observed in the Pacific, where simulated ϵ_{Nd} is slightly too low, particularly at shallow depths (Fig. 5).

Deviations of simulated from observed $[Nd]_d$ and ϵ_{Nd} mostly are of limited spatial extent. For instance, $[Nd]_d$ is

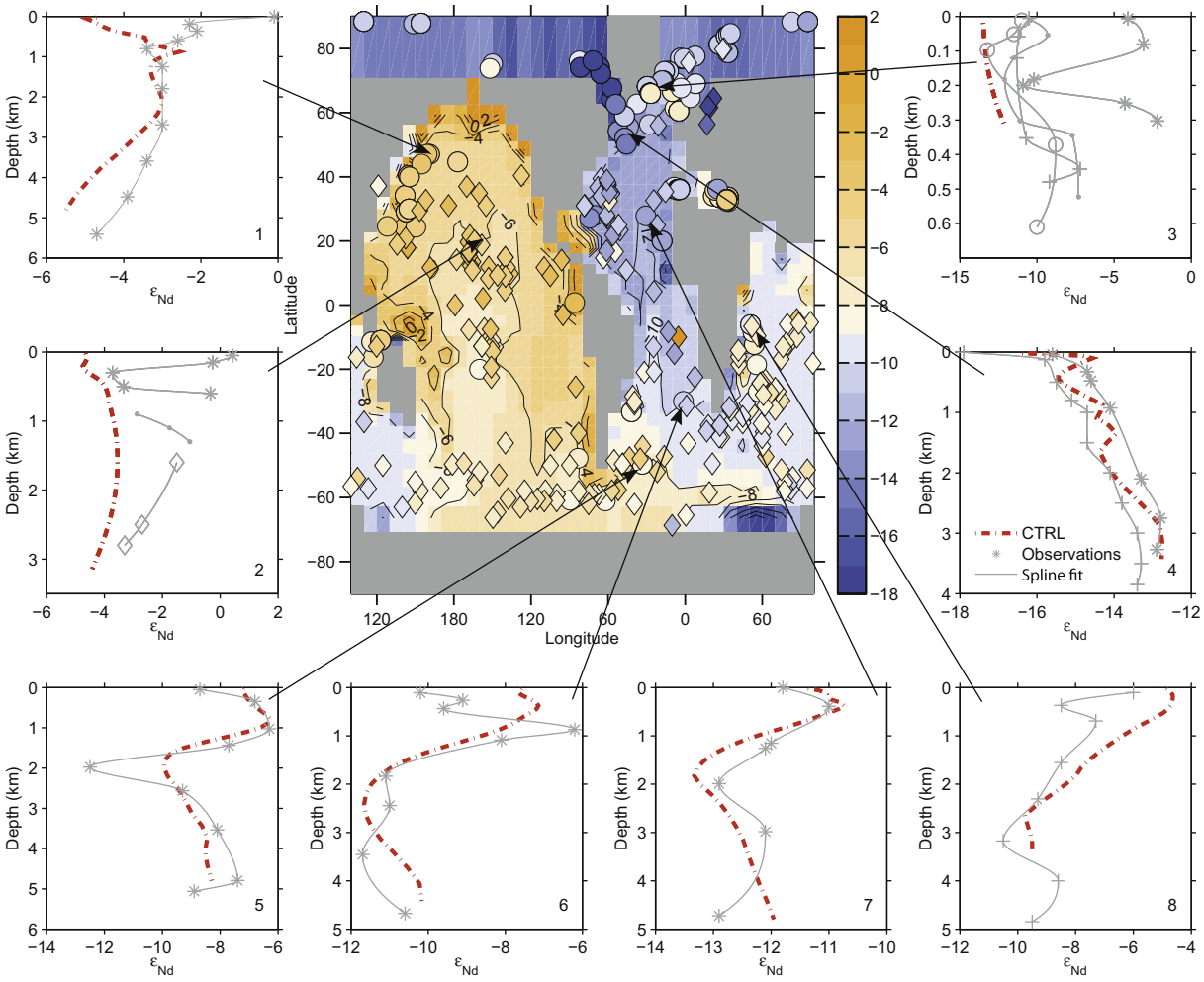

Fig. 9. Global map of ϵ_{Nd} at the sea floor (i.e., in the lowermost box of the model, central panel), obtained with CTRL. Seawater observations (colored circles) between the seafloor and 500 m above the depth of the corresponding grid cell, as well as ϵ_{Nd} measured on manganese crusts (colored diamonds, Frank, 2002), are superimposed using the same colorcoding. Profiles in adjacent panels show observed and simulated values of ϵ_{Nd}. Different markers indicate different observations. Observations were fitted using a cubic spline, arrows indicate the approximate location of each profile.

too high in the Arctic Ocean and too low below the Saharan dust plume. Regarding ϵ_{Nd}, rather regional features, e.g., close to Hawaii, or close to the coast in the Northeast Pacific, are not captured by the model. The inability of the model to capture such rather small-scale features is probably due to its low resolution and also due to the crude approximation of the sources of Nd. However, altogether the model is not only successful in simulating the global pattern of both $[Nd]_d$ and ϵ_{Nd}, but also simulates single open ocean profiles of both $[Nd]_d$ and ϵ_{Nd} quite well. Furthermore, the model successfully simulates ϵ_{Nd} of the main water masses (NADW, AABW, AAIW). We interpret the reasonable performance of our CTRL as an indication, that the model captures the main processes of the oceanic Nd-cycle.

In addition, Fig. 10 indicates that the general pattern of ϵ_{Nd} in southward and northward flowing watermasses in the Atlantic covaries with salinity, which corroborates the water mass property of ϵ_{Nd}. However, Fig. 10 suggests that ϵ_{Nd} and salinity do not match exactly. Compared to salinity, ϵ_{Nd} is shifted to greater depths. This offset results from the effect of reversible scavenging. Nd is adsorbed onto particle surfaces and is desorbed and released to seawater again if particles dissolve, thus leading to a downward transport of ϵ_{Nd}. We found the magnitude of the offset to depend on the choice of $[Nd]_p/[Nd]_d$ (not shown). If reversible scavenging was neglected, ϵ_{Nd} would match with salinity (while the interbasin-gradient decreased at the same time). In contrast, larger $[Nd]_p/[Nd]_d$ increased the mismatch of ϵ_{Nd} and $[Nd]_d$ with observations.

3.3. Varying f_{bs}

As mentioned above, the magnitude of the boundary source (f_{bs}) has been discussed in previous studies and different values have been estimated (Tachikawa et al., 2003; Arsouze et al., 2009). In this section, we examine the effect of halfing and doubling the magnitude of f_{bs} on $[Nd]_d$ and

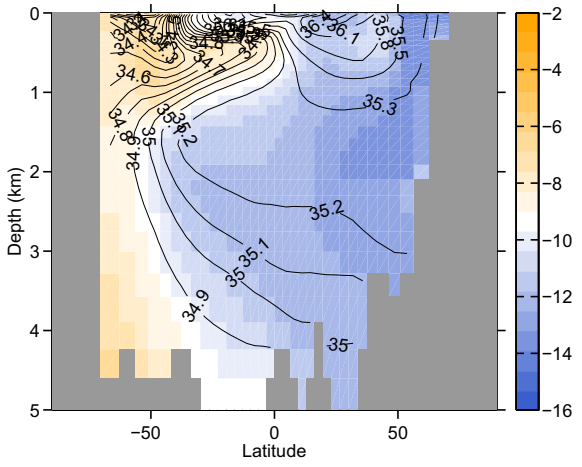

Fig. 10. Simulated ϵ_{Nd} (colored) and salinity (contours) in an Atlantic cross-Section (20–30 °W). ϵ_{Nd} covaries with salinity in the Atlantic, indicating the water mass property of ϵ_{Nd}.

ϵ_{Nd} in detail (experiments BS05 and BS20, Table 3). Cross-sections in Figs. 11 and 12 show simulated $[Nd]_d$ (a) and ϵ_{Nd} (c), as well as differences to the CTRL (b,d).

Varying the magnitude of f_{bs} affects the abililty of the model to simulate $[Nd]_d$ consistent with observations. In experiments BS05 and BS20, deviations from observations are larger ($J_{[Nd]_d}$), and a smaller fraction of observations of $[Nd]_d$ is simulated within ± 10 pmol kg^{-1} (J_1), while neither the fraction of ϵ_{Nd} which is simulated within ± 3 ϵ_{Nd}-units (J_2) is affected nor is $J_{\epsilon_{Nd}}$ (J_1 and J_2, Table 3). Cross-sections of $[Nd]_d$ (Fig. 11a–d) indicate decreased (increased) $[Nd]_d$ throughout the ocean, particularly in depths below the surface layers. In surface layers above ≈200 m, and particularly in regions where convection takes place, $[Nd]_d$ is less affected (Fig. 11b and d). Compared to observations, simulated $[Nd]_d$ at depths below 200–300 m is too low (large) if f_{tot} is decreased (increased), whereas $[Nd]_d$ at shallower depths is still within the observational range (Fig. 11a and c). Despite the considerable effect a decrease (increase) in f_{bs} exerts on $[Nd]_d$ below shallow layers, the nutrient-like pattern of increasing $[Nd]_d$ with depth and along the circulation pathway is well pronounced in both experiments. Regarding ϵ_{Nd} only a small effect can be observed in both experiments in cross sections (Fig. 12a–d). Effects on ϵ_{Nd} are largest in surface layers of the Atlantic (Fig. 12b and d). ϵ_{Nd} at the sea floor below the open ocean is almost unaffected (not shown). As the efficiency of the sink is not affected by an increase (decrease) of f_{bs}, the Nd inventory increases (decreases) in experiments BS05 (BS20), and τ_{Nd} remains constant (Table 3).

As in experiments BS05 (BS20) the decrease (increase) in f_{bs} is globally uniform, it does not affect the relative distribution of ^{143}Nd and ^{144}Nd, and thus ϵ_{Nd}. However, due to changes in the magnitude, the relationship between individual sources changes. This affects deep water masses, and the sea floor only to a small extent, but is restricted to the surface layers where Nd sources from dust and rivers add to

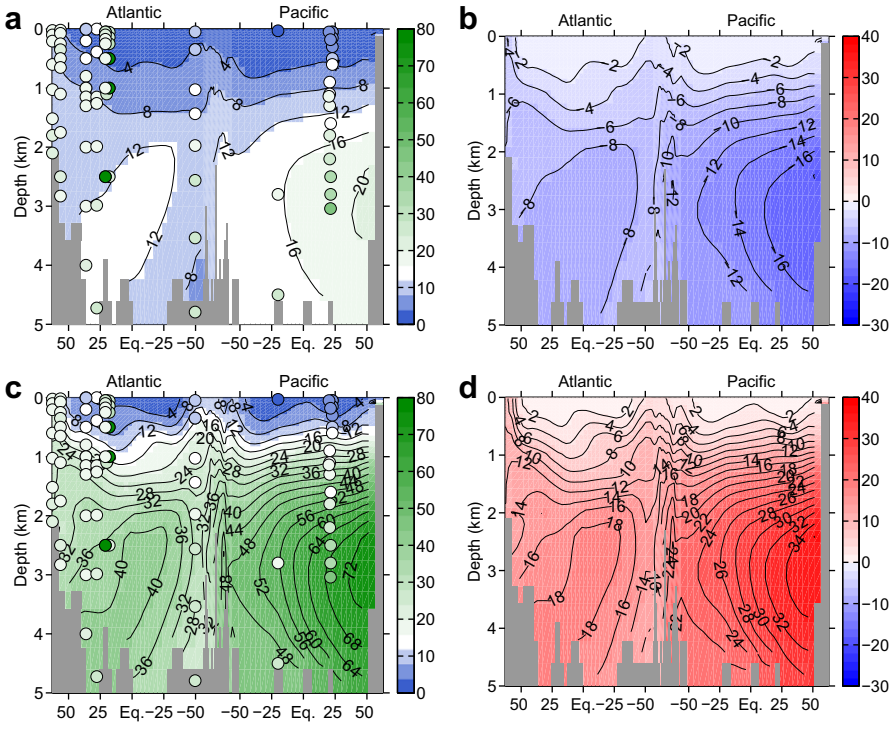

Fig. 11. Vertical sections, of $[Nd]_d$ along a track from the North Atlantic to the North Pacific (as indicated in Fig. 1a). Shown are results from experiments BS05, and BS20 (a and c) as well as differences between the CTRL and the corresponding experiment (BS05-CTRL, and BS20-CTRL, respectively, b and d). Observations of $[Nd]_d$ are superposed as colored circles using the same color scale in panels a and c. See Table 3 for further information on the experimental setup.

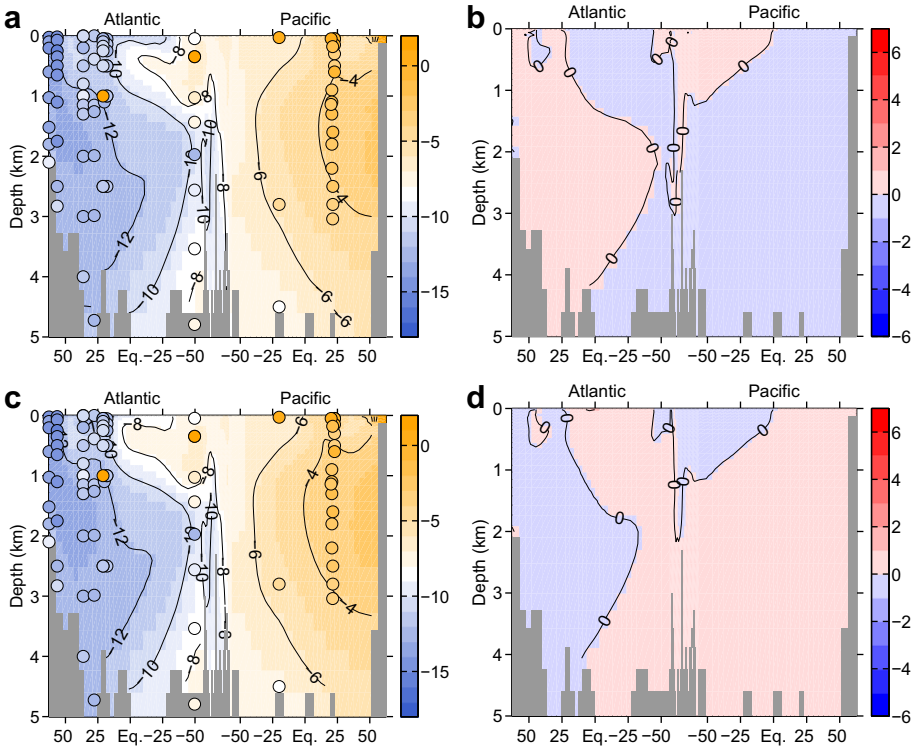

Fig. 12. Vertical sections, of ϵ_{Nd} along a track from the North Atlantic to the North Pacific (as indicated in Fig. 1a). Shown are results from experiments BS05, and BS20 (a and c) as well as differences between the CTRL and the corresponding experiment (BS05-CTRL, and BS20-CTRL, respectively, b and d). Observations of ϵ_{Nd} are superposed as colored circles using the same color scale in panels a and c. See Table 3 for further information on the experimental setup.

the Nd-budget. Regarding ϵ_{Nd}, results of experiments BS05 and BS20 therefore rather point to the sensitivity of ϵ_{Nd} to changes in the relationship between individual Nd sources.

3.4. Varying $[Nd]_p/[Nd]_d$

In experiments PD05 and PD20 we multiplied $[Nd]_p/[Nd]_d$ by a factor of 0.5 and 2. This is equivalent to a multiplication of each K-value, as $K_i^j \cdot R_i = [Nd]_{p,i}^j/[Nd]_d^j$, with constant R_i (Eq. 9). Accordingly, $[Nd]_p/[Nd]_d$ takes values of 5×10^{-4} and 2×10^{-3} in experiments PD05 and PD20, respectively (Table 3). The ratio between the individual K-values remains unchanged. Cross-sections of $[Nd]_d$ and ϵ_{Nd} are shown in Figs. 13 and 14. Profiles of ϵ_{Nd} as well as differences in ϵ_{Nd} at the sea floor are shown in Fig. 15a, 15b.

$[Nd]_p/[Nd]_d$ considerably affects the ability of the model to simulate observations of $[Nd]_d$ and ϵ_{Nd} consistent with observations (Fig. 2). In experiments PD05 and PD20, $J_{[Nd]_d}$ and $J_{\epsilon_{Nd}}$ are larger than in the CTRL (Table 3). 50% and 79% of the observations of $[Nd]_d$ and ϵ_{Nd}, are simulated within ± 10 pmol kg^{-1}, and ± 3 ϵ_{Nd}-units deviation in experiment PD05. Values are 51% and 78% in experiment PD20 (Table 3). The mean residence time in experiment PD05 increases from ≈700 to ≈1270 yr (Table 3). $[Nd]_d$ increases at all depths in Atlantic and Pacific basins, although largest changes occur in the deep Pacific (Fig. 13b). In experiment PD20, τ_{Nd} decreases to ≈330 yr (Table 3), and $[Nd]_d$ decreases throughout the ocean (Fig. 13d). However, the nutrient-like pattern is preserved in both experiments; $[Nd]_d$ increases with depth, and largest values are observed in the deep North Pacific (Fig. 13a and b).

Heterogeneity of ϵ_{Nd} within the water column and between individual basins is more (less) pronounced in the case of increased (decreased) $[Nd]_p/[Nd]_d$ (Fig. 15a, 15b profiles #1–8). Compared to the CTRL, in experiment PD05 ϵ_{Nd} is more positive in the North Atlantic (1.5 ϵ_{Nd}-units), and more negative (2 ϵ_{Nd}-units) in the North Pacific. Similar, but contrary effects on ϵ_{Nd} are observed in experiment PD20, where ϵ_{Nd} is more negative in the North Atlantic (1.5 ϵ_{Nd}-units) and more positive in the North Pacific (2.5 ϵ_{Nd}-units). These changes also affect ϵ_{Nd} of main water masses in the Atlantic (Fig. 14), and can be observed particularly well in Atlantic "zig zag"-profiles (Fig. 15a, 15b profiles #5 and 6).

According to Eq. (14), an increase (decrease) in $[Nd]_p/[Nd]_d$ shifts the equilibrium between dissolved and particle-associated concentrations, i.e., it discriminates (favors) dissolved against particle-associated Nd, respectively. A shift in $[Nd]_p/[Nd]_d$ corresponds to a change in the efficiency of the sink of Nd, as a larger (smaller) fraction of Nd is removed from the water column by settling of particles and burial in the sediments. This leads to a more (less) pronounced increase of $[Nd]_d$ along the circulation pathway, i.e., in larger (smaller) concentrations in deep water masses, particularly in the deep North Pacific and is reflected in lar-

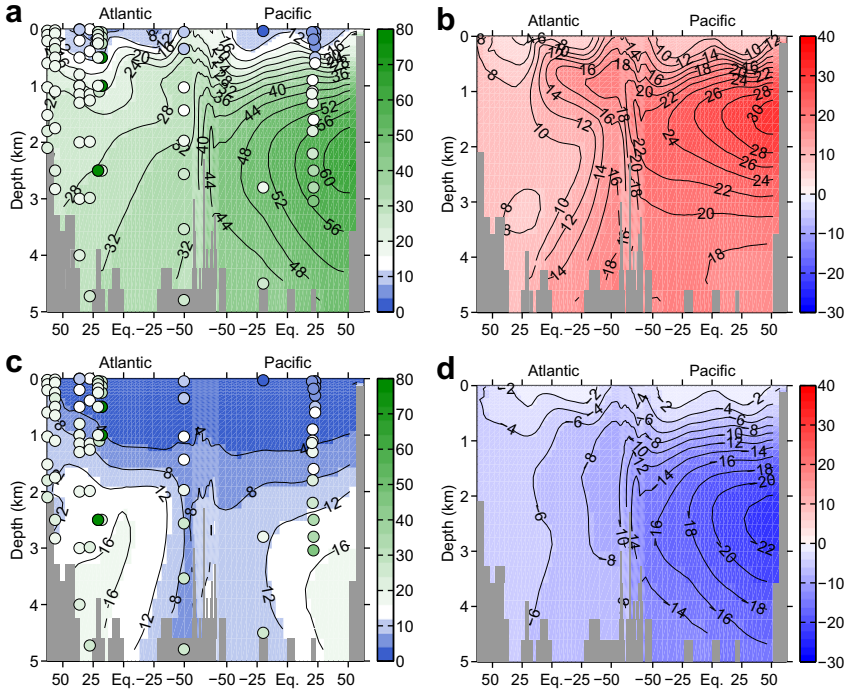

Fig. 13. Vertical sections, of $[Nd]_d$ along a track from the North Atlantic to the North Pacific (as indicated in Fig. 1a). Shown are results from experiments PD05, and PD20 (a and c) as well as differences between the CTRL and the corresponding experiment (PD05-CTRL, and PD20-CTRL, respectively, b and d). Observations of $[Nd]_d$ are superposed as colored circles using the same color scale in panels a and c. See Table 3 for further information on the experimental setup.

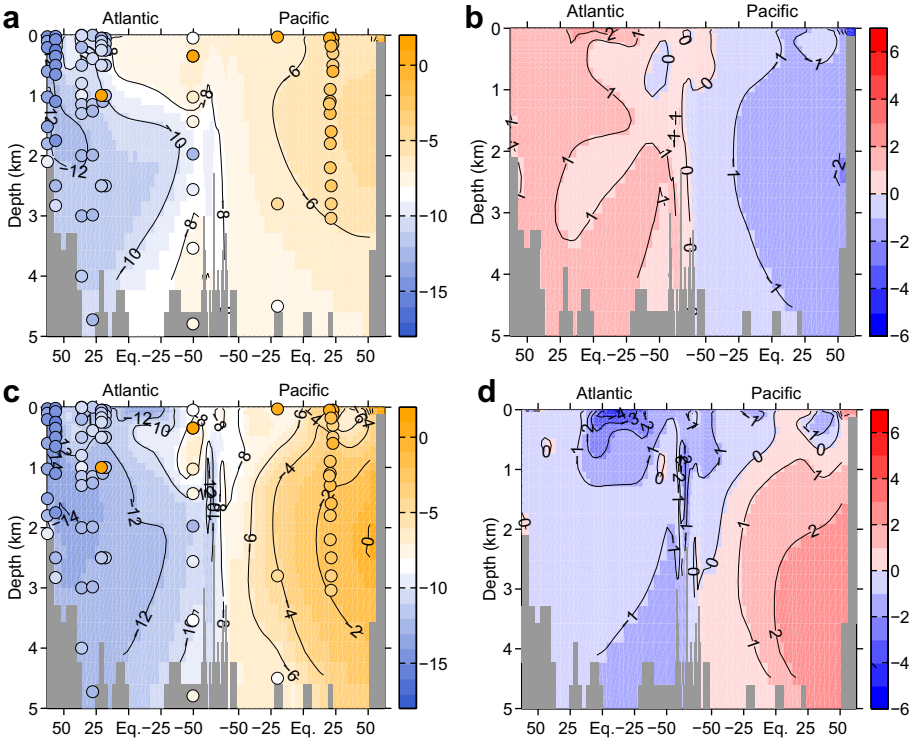

Fig. 14. Vertical sections, of ϵ_{Nd} along a track from the North Atlantic to the North Pacific (as indicated in Fig. 1a). Shown are results from experiments PD05, and PD20 (a and c) as well as differences between the CTRL and the corresponding experiment (PD05-CTRL, and PD20-CTRL, respectively, b and d). Observations of ϵ_{Nd} are superposed as colored circles using the same color scale in panels a and c. See Table 3 for further information on the experimental setup.

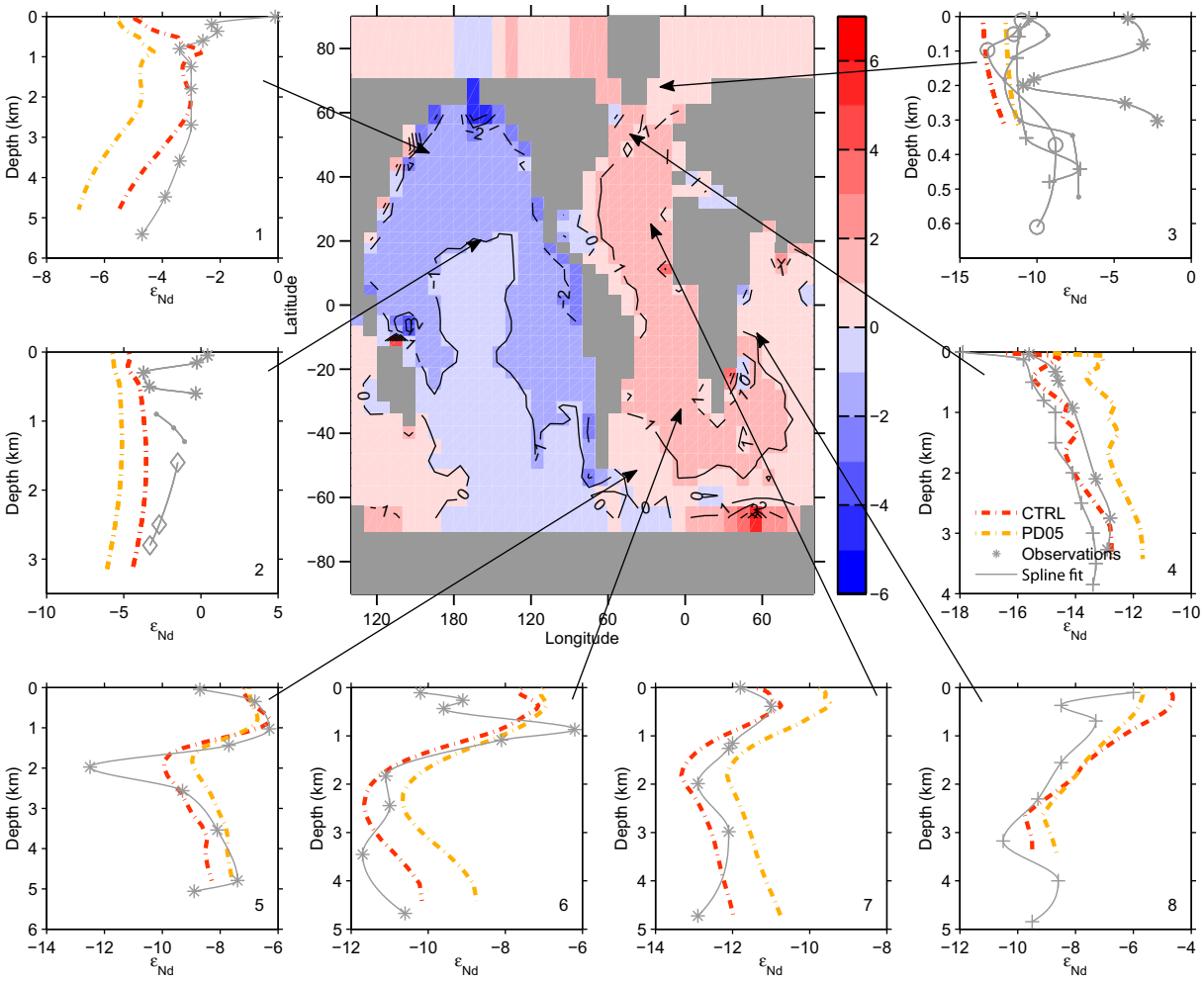

Fig. 15a. Global map of differences in ϵ_{Nd} at the sea floor (central panel, PD05-CTRL, see Table 3 for further information on the experimental setup). Profiles in adjacent panels show observed and simulated ϵ_{Nd} (CTRL and PD05). Different markers indicate different observations. Observations were fitted using a cubic spline, arrows indicate the approximate location of each profile.

ger (smaller) mean residence time (1270 yr and 330 yr, respectively, Table 3). Besides affecting $[Nd]_d$, such a shift in the equilibrium between dissolved and particle-associated Nd, also affects ϵ_{Nd} of water masses: The signature of a certain water mass is transported further away from its source through advection if the reversible scavenging is less efficient, and vice versa. Therefore, the heterogeneity of ϵ_{Nd} within single profiles is less (more) pronounced if $[Nd]_p/[Nd]_d$ is decreased (increased).

Comparable to our results, Siddall et al., 2008 reported an effect of a change in $[Nd]_p/[Nd]_d$ on ϵ_{Nd} in the Pacific, but argued that the effect is less significant in the Atlantic due to the vigorous advective transport in this basin. In contrast, in our model we find a considerable effect of $[Nd]_p/[Nd]_d$ on ϵ_{Nd} throughout the ocean. We attribute this to differences in the approaches. Siddall et al., 2008 applied fixed boundary conditions for $[Nd]_d$ at the sea surface, which are not influenced by the change in $[Nd]_p/[Nd]_d$. As shown in Fig. 15a, in experiment PD05 also ϵ_{Nd} at the sea surface in the North Atlantic is affected. This change is then transported to greater depth by convection and advected southward in the NADW afterwards.

3.5. The boundary source as a unique source of Nd

In this section we examine the potential of the boundary source to serve as a unique source of Nd. Therefore, we omit input via rivers and dust, and, in order to keep the inventory of Nd constant, add f_{du} and f_{ri} to f_{bs} (Table 3). Cross-sections of simulated $[Nd]_d$ and ϵ_{Nd}, as well as differences to the CTRL are shown in Fig. 16 (panels a, c and b, d, respectively).

Simulated distributions of $[Nd]_d$ and ϵ_{Nd} slightly differ between CTRL and DR00 (not shown), and $J_{[Nd]_d}$ and $J_{\epsilon_{Nd}}$ in Table 3 indicate decreased performance for $[Nd]_d$ and ϵ_{Nd} in the DR00-experiment. Cross-sections of $[Nd]_d$ show somewhat smaller $[Nd]_d$ in the North Atlantic (Fig. 16). ϵ_{Nd} is more positive in shallow depths of the tropical and South Atlantic, where values of ϵ_{Nd} similar to ϵ_{Nd} in AAIW, extend to the surface. ϵ_{Nd} is almost unaffected at depths below ≈1 km (Fig. 16).

In the CTRL, dust and rivers account for about 10% of the global Nd-budget. This amount of Nd is not evenly distributed between individual basins. In contrast, the largest fraction of riverine Nd enters the ocean in the Atlantic

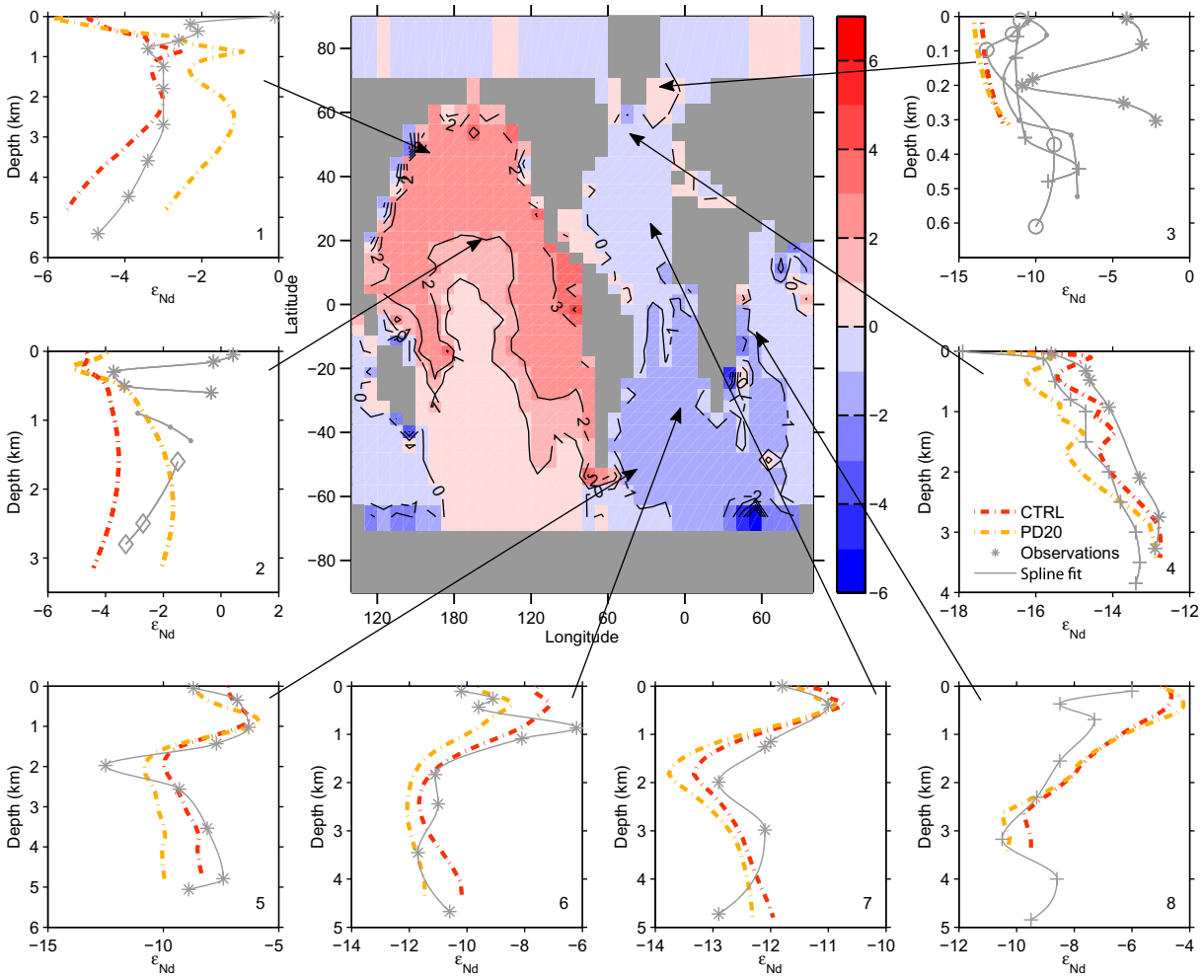

Fig. 15b. Global map of differences in ϵ_{Nd} at the sea floor (central panel, PD20-CTRL, see Table 3 for further information on the experimental setup). Profiles in adjacent panels show observed and simulated ϵ_{Nd} (CTRL and PD20). Different markers indicate different observations. Observations were fitted using a cubic spline, arrows indicate the approximate location of each profile.

(70% or 2.9×10^8 of 3.4×10^8 g Nd yr^{-1}). A similar pattern can be observed for dust (50%, or 1.3×10^8 of 2.6×10^8 g Nd yr^{-1}). Furthermore, input from dust and rivers is restricted to the uppermost box in the model, while the boundary source is represented by a globally uniform flux between the surface and 3000 m depth. Neglecting dust and rivers as a source of Nd, thus causes a shift in the distribution of sources among basins, i.e., causes decreased $[Nd]_d$ in the Atlantic and slightly increased $[Nd]_d$ in the Pacific.

Results from this experiment lead us to conclude, that despite their small contribution (about 10%) to the total flux of Nd, dust and rivers are components of the Nd cycle that need to be taken into account in order to simulate the spatial patterns of $[Nd]_d$ and in particular of ϵ_{Nd} in the upper 500 m of the water column, consistent with observations.

3.6. Effects of varying diapycnal diffusivity and Atlantic-to-Pacific freshwater flux on $[Nd]_d$ and ϵ_{Nd}

In ocean models, ocean overturning circulation is largely controlled by κ_D and $Fw_{Atl-Pac}$ (as well as wind strength). For both parameters, larger values result in a more vigorous circulation in the Atlantic, and also affect the strength of the overturning in the Pacific. In experiments where we varied κ_D (1.0; 3.5; 6.0; 10.0×10^{-5} m^{-2} s^{-1}, x-axis in Fig. 17) and $Fw_{Atl-Pac}$ (0.1; 0.15; 0.2; 0.3; 0.4 Sv, y-axis in Fig. 17), the strength of the Atlantic overturning circulation varies between about 14 and 28 Sv. Besides affecting the overturning strength, increasing $Fw_{Atl-Pac}$ also deepens the overturning cell in the North Atlantic. Furthermore, the strength of the anticlockwise overturning of southern sourced water in the deep Atlantic decreases for increasing $Fw_{Atl-Pac}$ (not shown).

The Bern3D ocean model has been tuned towards observed chlorofluorocarbon (CFC-11) inventories and deep ocean radiocarbon signatures in order to reproduce ventilation time scales of the thermocline and the deep ocean (Müller et al., 2006). The model yields reasonable results for values of $Fw_{Atl-Pac} = 0.15$ Sv and $\kappa_D = 1.0 \times 10^{-5}$ m^{-2} s^{-1}. This parametrisation results in an annual mean Atlantic overturning circulation of about 16.2 Sv, which is similar to observations (Ganachaud and Wunsch, 2000; Talley et al., 2003). However, Fig. 17

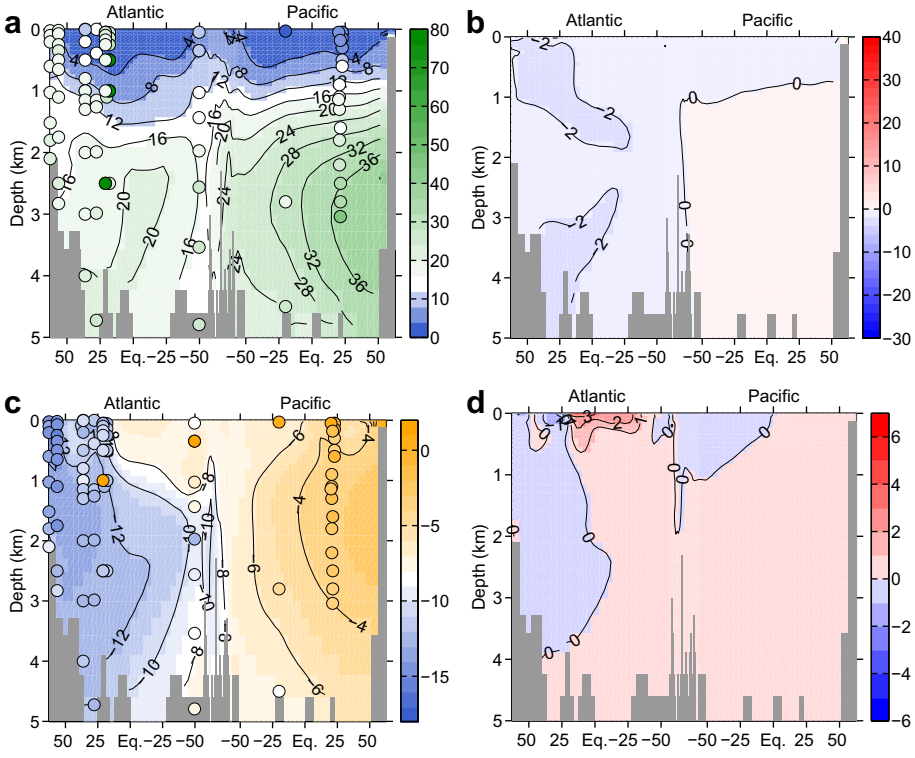

Fig. 16. Vertical sections, of $[Nd]_d$ (top) and ϵ_{Nd} (bottom) along a track from the North Atlantic to the North Pacific (as indicated in Fig. 1a). Shown are results from DR00 (a and c), as well as differences to the CTRL (DR00-CTRL, b and d). Observations of $[Nd]_d$ and ϵ_{Nd} are superposed as colored circles using the same color scale in panels a and c. See Table 3 for further information on the experimental setup.

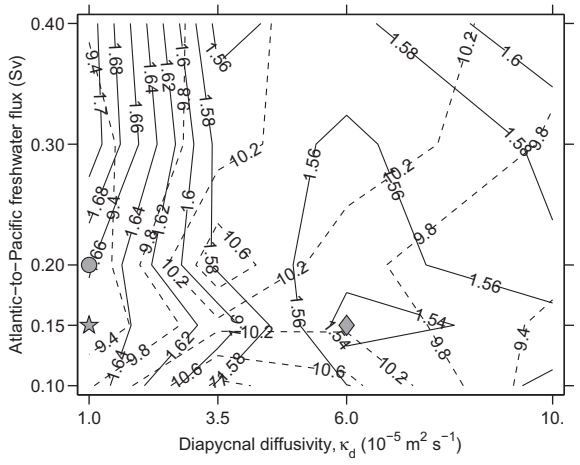

Fig. 17. Global average deviations of simulated from observed $[Nd]_d$ and ϵ_{Nd}, for different parametrisations of the physical ocean model. $J_{[Nd]_d}$ (dashed) and $J_{\epsilon_{Nd}}$ (solid) are calculated following Eq. 15, units are pmol kg^{-1} and ϵ_{Nd}-units. Variations in $J_{[Nd]_d}$ and $J_{\epsilon_{Nd}}$ indicate the sensitivity of the model to different values for the diapycnal diffusivity (κ_D, x-axis) and the Atlantic-to-Pacific freshwater flux ($Fw_{Atl-Pac}$, y-axis). Combinations of parameters of κ_D and $Fw_{Atl-Pac}$ for which $J_{[Nd]_d}$ and $J_{\epsilon_{Nd}}$ reach minima are indicated by a filled circle and diamond, respectively. The setup of CTRL is indicated as filled hexagram.

indicates that $J_{[Nd]_d}$ and $J_{\epsilon_{Nd}}$ are not at their minima for this setup.

Both $[Nd]_d$ and ϵ_{Nd} are affected considerably in the Atlantic and the Pacific basin, in experiments where the largest changes are applied to κ_D ($\kappa_D = 10^{-4}$ m^{-2} s^{-1}) and $Fw_{Atl-Pac}$ ($Fw_{Atl-Pac} = 0.4$ Sv, not shown). Nevertheless, overall effects on $[Nd]_d$ and ϵ_{Nd} are small, if compared to effects resulting from changes in the nature and magnitude of sources and sinks of Nd (Figs. 2 and 17, respectively).

4. DISCUSSION AND SUMMARY

In this study, we presented an approach to simulate the global oceanic distribution of the Nd isotopes ^{143}Nd and ^{144}Nd, as well as results from a number of sensitivity experiments. We quantified sensitivities of $[Nd]_d$ and ϵ_{Nd} to model parameters and source/sink distributions, thus considerably extending earlier modelling efforts of Nd-isotopes of Siddall et al., 2008 and Arsouze et al., 2009. The comprehensive approach and the high computational efficiency of our model allowed us to study sensitivities of the marine Nd cycle in detail. Previous studies have been restricted in doing so either by the chosen approach or by computational costs. These experiments further our understanding of Nd sources and sinks as well as its internal cycling. Beyond that, our model does not allow to further elucidate processes involved e.g., in the boundary source, and the discussion of its exact nature is beyond the objective of this study. Instead, we refer to available studies where a range of processes has been discussed (e.g., van de Flierdt et al., 2004; Lacan and Jeandel, 2005; Johannesson and Burdige, 2007).

We systematically explored the parameter space of the two major tuning parameters of the Nd module, and quantified the performance of each model set-up by the use of cost functions $J_{[Nd]_d}$ and $J_{\epsilon_{Nd}}$. From our simulations, we found it difficult to make a best choice for the CTRL, based on $J_{[Nd]_d}$ and $J_{\epsilon_{Nd}}$ alone. It was not possible to find a parametrisation which produces minima in both, $J_{[Nd]_d}$ and $J_{\epsilon_{Nd}}$. Any choice of a CTRL constituted some compromise. For the CTRL we chose the parametrisation for which $J_{\epsilon_{Nd}}$ produces a minimum and demonstrated its ability to capture many of the features observed in the distribution of $[Nd]_d$ and ϵ_{Nd}. Quality measures indicate a comparable or even higher degree of consistency with observations as reported by Arsouze et al., 2009. This is noteworthy as these authors used a higher resolved OGCM.

Our success in simulating both $[Nd]_d$ and ϵ_{Nd} at the same time, supports findings of previous studies in various aspects: First, input of Nd from dust and rivers is of minor importance. Instead, the major fraction of Nd enters the ocean across the sediment-seawater interface, i.e., the continental margins (Tachikawa et al., 2003; Arsouze et al., 2009). In the CTRL, about 90% of the total Nd are delivered to the ocean through f_{bs}, while 6% and 4% enter the ocean via river discharge and atmospheric dust flux, respectively. However, experiment DR00 indicates that, while contributing only about 10% of the total source, Nd input from dust and rivers is an important component of the Nd cycle and consistency between simulated and observed $[Nd]_d$ and ϵ_{Nd}, particularly in the upper 500 m of the water column, is larger if input from dust and rivers is taken into account. Compared to previous studies of Tachikawa et al., 2003 and Arsouze et al., 2009, f_{bs} in our CTRL is slightly smaller. However, as Tachikawa et al., 2003 used a 10-box model, a direct comparison of the values may be difficult. Regarding the study of Arsouze et al., 2009, a potential explanation for the discrepancy in the values of f_{bs} was the efficiency of the transport of Nd to the sediment by settling particles, which directly depends on $[Nd]_p/[Nd]_d$. A comparison of these values is complicated by differences in the biogeochemical models.

Second, neodymium concentrations can be simulated consistent with observations if reversible scavenging is taken into account (Siddall et al., 2008). However, in contrast to this study, Siddall et al., 2008 optimise *K*-values for each particle type (POC, opal, $CaCO_3$, and dust) and thus allow for the possibility of preferential scavenging. For example they get best results if scavenging of Nd on POC is neglected. We did not allow for preferential scavenging and from our simulations found a value for $[Nd]_p/[Nd]_d$ of about 0.001 to yield reasonable results. This value does not differ much from the few available observations (e.g., Jeandel et al., 1995), and is similar to values reported by Arsouze et al., 2009.

Third, ϵ_{Nd} covaries with salinity, thus underlining the water-mass property of ϵ_{Nd} (von Blanckenburg, 1999; Jones et al., 2008). We found the degree of congruence in the spatial pattern of ϵ_{Nd} and salinity to depend on the efficiency of downward transport of Nd by settling particles, and thus on the parametrisation of the reversible scavenging.

Strong interbasin gradients, such as those observed for ϵ_{Nd}, can be built up only if τ_{Nd} is similar to the mean ocean mixing time (e.g., Goldstein and Hemming, 2003). Our CTRL complies with this requirement as τ_{Nd} ($\approx$700 yr) is slightly shorter than the mean ocean mixing time of the model ($\approx$830 yr, obtained with an ideal age tracer). Furthermore, both values are comparable to available estimates (e.g., Broecker and Peng, 1982; Tachikawa et al., 1999; Frank, 2002; Goldstein and Hemming, 2003; Lacan and Jeandel, 2005), and τ_{Nd} is similar to, although slightly larger than, estimates of previous modelling studies: $\approx$500 yr in Tachikawa et al., 2003, between 10–30 and 500 yr in Siddall et al., 2008 and between 125 and 640 yr in Arsouze et al., 2009. The fact that different approaches yield similar values supports such a range for τ_{Nd}.

We carried out further sensitivity tests where we varied the pattern and the strength of the simulated ocean circulation. Thus, we have shown that, apart from the parametrisation of the Nd module, the simulated distribution of $[Nd]_d$ and ϵ_{Nd} also depends on the simulated ocean circulation. However, within the range examined, effects of circulation strength and patterns on $[Nd]_d$ and ϵ_{Nd} are relatively small if compared to effects observed for variations in $[Nd]_p/[Nd]_d$ and f_{bs}. This points to the importance of an adequate representation of Nd sources and sinks.

One of the next steps would be the implementation of Nd isotopes into a sediment module that can be coupled to an ocean model. However, to date this is still limited by the poor understanding of processes affecting Nd isotopes in sediments. An improved understanding of processes associated with the boundary source, as well as of processes in sediments, potentially affecting $[Nd]_d$ and ϵ_{Nd}, is thus needed. Moreover, we note that the evaluation of model performance in general would benefit from more observations of $[Nd]_d$ and ϵ_{Nd}, particularly in regions where only few observations are currently available (e.g., in the Southern Ocean). Furthermore, more observations of particle-associated Nd concentrations would permit a more thorough evaluation of the internal cycling of Nd. Fortunately, new insight into marine biogeochemical processes associated with the cycling of trace elements and isotopes such as Nd can be expected from the international GEOTRACES program in the near future (SCOR Working Group, 2007).

Overall, the success in simulating both $[Nd]_d$ and ϵ_{Nd}, with the presented approach and within a coarse resolution ocean circulation model, makes it a powerful tool for the further exploration of the paleoceanographic potential of ϵ_{Nd}, in particular investigating transient experiments.

ACKNOWLEDGEMENTS

This work was funded through the Marie Curie Research Training Network NICE (Network for Ice sheet and Climate Evolution). F.J. acknowledges support by the European Project on Ocean Acidification (EPOCA, FP7/2007-2013; No. 211384) and Past4Future (Grant No. 243908). M.S. is supported by a fellowship from the Research Council UK and by the University of Bristol. We thank T. Tschumi, P. Parekh, and S. Ritz for their contributions in the development of the Bern3D model, and K. Bieri for technical assistance. We are also grateful to Catherine Jeandel,

Martin Frank and an anonymous reviewer, whose valuable comments led to significant improvements in the manuscript.

REFERENCES

Andersson P. S., Porcelli D., Frank M., Björk G., Dahlqvist R. and Gustafsson O. (2008) Neodymium isotopes in seawater from the barents sea and fram strait Arctic–Atlantic gateways. *Geochimica et Cosmochimica Acta* **72**(12), 2854–2867.

Arsouze T., Dutay J. C., Lacan F. and Jeandel C. (2007) Modeling the neodymium isotopic composition with a global ocean circulation model. *Chemical Geology* **239**, 165–177.

Arsouze T., Dutay J.-C., Lacan F. and Jeandel C. (2009) Reconstructing the Nd oceanic cycle using a coupled dynamical biogeochemical model. *Biogeosciences* **6**(12), 2829–2846.

Aumont O. and Bopp L. (2006) Globalizing results from ocean in situ iron fertilization studies. *Global Biogeochemical Cycles* **20**, GB2017.

Bacon M. and Anderson R. (1982) Distribution of thorium isotopes between dissolved and particulate forms in the deep sea. *Journal of Geophysical Research* **87**, 2045–2056.

Bertram C. and Elderfield H. (1993) The geochemical balance of the rare Earth elements and neodymium isotopes in the oceans. *Geochimica et Cosmochimica Acta* **57**(9), 1957–1986.

Broecker W. S. and Peng T.-H. (1982) Tracers in the Sea. Eldigio Press.

Doney S. C., Lindsay K., Fung I. and John J. (2006) Natural variability in a stable 1000 year global coupled climate-carbon cycle simulation. *Journal of Climate* **19**, 3033–3054.

Edwards N. and Marsh R. (2005) Uncertainties due to transport-parameter sensitivity in an efficient 3-d ocean-climate model. *Climate Dynamics* **24**, 415–433.

Elderfield H. and Greaves M. J. (1982) The rare Earth elements in seawater. *Nature* **296**, 214–219.

Elderfield H. and Sholkovitz E. (1987) Rare Earth elements in the pore waters of reducing nearshore sediments. *Earth and Planetary Science Letters* **82**(3–4), 280–288.

Elderfield H., Upstill-Goddard R. and Sholkovitz E. (1990) The rare Earth elements in rivers, estuaries, and coastal seas and their significance to the composition of ocean waters. *Geochimica et Cosmochimica Acta* **54**(4), 971–991.

Frank M. (2002) Radiogenic isotopes: Tracers of past ocean circulation and erosional input. *Review of Geophysics* **40**(1), 1001.

Frank M., Whiteley N., Kasten S., Hein J. R. and O'Nions K. (2002) North Atlantic deep water export to the southern ocean over the past 14 myr: evidence from nd and pb isotopes in ferromanganese crusts. *Paleoceanography* **17**(2), 1022.

Ganachaud A. and Wunsch C. (2000) Improved estimates of global ocean circulation heat, transport and mixing from hydrographic data. *Nature* **408**, 453–457.

Gangstø R., Joos F. and Gehlen M. (2011) Sensitivity of pelagic calcification to ocean acidification. *Biogeosciences* **8**(2), 433–458.

Goldstein S. J. and Jacobsen S. B. (1987) The Nd and Sr isotopic systematics of river-water dissolved material: implications for the sources of nd and sr in seawater. *Chemical Geology: Isotope Geoscience section* **66**(3-4), 245–272.

Goldstein S. L. and Hemming S. R. (2003) Long-lived isotopic tracers in oceanography, paleoceanography, and ice-sheet dynamics. In *Treatise on Geochemistry* (ed. H. Elderfield). Elsevier, Oxford.

Goldstein S., O'Nions R. and Hamilton P. (1984) A Sm-Nd isotopic study of atmospheric dusts and particulates from major river systems. *Earth and Planetary Science Letters* **70**(2), 221–236.

Greaves M., Elderfield H. and Sholkovitz E. (1999) Aeolian sources of rare Earth elements to the western Pacific ocean. *Marine Chemistry* **68**(1–2), 31–38.

Greaves M., Statham P. and Elderfield H. (1994) Rare Earth element mobilization from marine atmospheric dust into seawater. *Marine Chemistry* **46**(3), 255–260.

Grousset F., Biscaye P., Zindler A., Prospero J. and Chester R. (1988) Neodymium isotopes as tracers in marine sediments and aerosols: North Atlantic. *Earth and Planetary Science Letters* **87**(4), 367–378.

Grousset F. E., Parra M., Bory A., Martinez P., Bertrand P., Shimmield G. and Ellam R. M. (1998) Saharan wind regimes traced by the Sr–Nd isotopic composition of subtropical Atlantic sediments: last glacial maximum vs. today. *Quaternary Science Reviews* **17**(4–5), 395–409.

Gutjahr M., Frank M., Stirling C., Keigwin L. and Halliday A. (2008) Tracing the Nd isotope evolution of North Atlantic deep and intermediate waters in the western North Atlantic since the last glacial maximum from blake ridge sediments. *Earth and Planetary Science Letters* **266**(1–2), 61–77.

Haley B. A., Klinkhammer G. P. and McManus J. (2004) Rare Earth elements in pore waters of marine sediments. *Geochimica et Cosmochimica Acta* **68**(6), 1265–1279.

Henderson G., Heinze C., Anderson R. and Winguth A. (1999) Global distribution of the Th-230 flux to ocean sediments constrained by GCM modelling. *Deep-Sea Research Part I - Oceanographic Research Papers* **46**(11), 1861–1893.

Jacobsen S. B. and Wasserburg G. (1980) Sm–Nd isotopic evolution of chondrites. *Earth and Planetary Science Letters* **50**, 139–155.

Jeandel C. (1993) Concentration and isotopic composition of Nd in the South Atlantic ocean. *Earth and Planetary Science Letters* **117**(3–4), 581–591.

Jeandel C., Arsouze T., Lacan F., Techine P. and Dutay J.-C. (2007) Isotopic Nd compositions and concentrations of the lithogenic inputs into the ocean: a compilation, with an emphasis on the margins. *Chemical Geology* **239**(1–2), 156–164.

Jeandel C., Bishop J. K. and Zindler A. (1995) Exchange of neodymium and its isotopes between seawater and small and large particles in the Sargasso sea. *Geochimica et Cosmochimica Acta* **59**(3), 535–547.

Johannesson K. H. and Burdige D. J. (2007) Balancing the global oceanic neodymium budget: evaluating the role of groundwater. *Earth and Planetary Science Letters* **253**(1–2), 129–142.

Jones K. M., Khatiwala S. P., Goldstein S. L., Hemming S. R. and van de Flierdt T. (2008) Modeling the distribution of nd isotopes in the oceans using an ocean general circulation model. *Earth and Planetary Science Letters* **272**(3–4), 610–619.

Kalnay E., Kanamitsu M., Kistler R., Collins W., Deaven D., Gandin L., Iredell M., Saha S., White G., Woollen J., Zhu Y., Leetmaa A., Reynolds R., Chelliah M., Ebisuzaki W., Higgins W., Janowiak J., Mo K. C., Ropelewski C., Wang J., Jenne R. and Joseph D. (1996) The NCEP/NCAR 40-year reanalysis project. *Bulletin of the American Meteorological Society* **77**(3), 437–471.

Lacan F. and Jeandel C. (2005) Neodymium isotopes as a new tool for quantifying exchange fluxes at the continent-ocean interface. *Earth and Planetary Science Letters* **232**(3–4), 245–257.

Levitus S. and Boyer T. (1994) Temperature, *World Ocean Atlas* **4**.

Levitus S., Burgett R. and Boyer T. (1994) Salinity, *World Ocean Atlas* **3**.

Luo C., Mahowald N. M. and del Corral J. (2003) Sensitivity study of meteorological parameters on mineral aerosol mobilization,

transport, and distribution. *Journal of Geophysical Research* **108**(D15), 4447.

Lynch-Stieglitz J. (2003) Tracers of past ocean circulation. In *Treatise on Geochemistry* (eds. H.D. Holland and K.K. Turekian). Elsevier, Oxford, pp. 433–451.

Magill J., Pfennig G. and Galy J. (2006) *Chart of the Nuclides*. European Commission, seventh ed., Joint Research Centre, Karlsruhe.

Maier-Reimer E., Kriest I., Segschneider J. and Wetzel P. (2005) The Hamburg ocean carbon cycle model hamocc5.1 – Technical description release 1.1, *Technical Report*, Max Planck Institute for Meteorology, Hamburg.

Marchal O., Francois R., Stocker T. F. and Joos F. (2000) Ocean thermohaline circulation and sedimentary Pa-231/Th-230 ratio. *Paleoceanography* **15**, 625–641.

Martin J., Knauer G., Karl D. and Broenkow W. (1987) Vertex: carbon cycling in the northeast pacific. *Deep Sea Research* **34**, 267–285.

Müller S. A., Joos F., Edwards N. R. and Stocker T. F. (2006) Water mass distribution and ventilation time scales in a cost-efficient, three-dimensional ocean model. *Journal of Climate* **19**, 5479–5499.

Müller S. A., Joos F., Plattner G.-K., Edwards N. R. and Stocker T. F. (2008) Modeled natural and excess radiocarbon: sensitivities to the gas exchange formulation and ocean transport strength. *Global Biogeochemical Cycles* **22**, GB3011.

Oka A., Hasumi H., Obata H., Gamo T. and Yamanaka Y. (2009) Study on vertical profiles of rare Earth elements by using an ocean general circulation model. *Global Biogeochemical Cycles* **23**, GB4025.

Pahnke K., Goldstein S. L. and Hemming S. R. (2008) Abrupt changes in antarctic intermediate water circulation over the past 25,000 years. *Nature Geoscience* **1**, 870–874.

Parekh P., Joos F. and Müller S. A. (2008) A modeling assessment of the interplay between aeolian iron fluxes and iron-binding ligands in controlling carbon dioxide fluctuations during Antarctic warm events. *Paleoceanography* **23**, PA4202.

Piepgras D. J. and Jacobsen S. B. (1988) The isotopic composition of neodymium in the North Pacific. *Geochimica et Cosmochimica Acta* **52**(6), 1373–1381.

Piepgras D. and Wasserburg G. (1987) Rare Earth element transport in the western North Atlantic inferred from Nd isotopic observations. *Geochimica et Cosmochimica Acta* **51**(5), 1257–1271.

Piotrowski A. M., Banakar V. K., Scrivner A. E., Elderfield H., Galy A. and Dennis A. (2009) Indian ocean circulation and productivity during the last glacial cycle. *Earth and Planetary Science Letters* **285**(1-2), 179–189.

Piotrowski A. M., Goldstein S. L., Hemming S. R. and Fairbanks R. G. (2004) Intensification and variability of ocean thermohaline circulation through the last deglaciation. *Earth and Planetary Science Letters* **225**, 205–220.

Piotrowski A. M., Goldstein S. L., Hemming R. S., Fairbanks R. G. and Zylberberg D. R. (2008) Oscillating glacial northern and southern deep water formation from combined neodymium and carbon isotopes. *Earth and Planetary Science Letters* **272**(1–2), 394–405.

Porcelli D., Andersson P. S., Baskaran M., Frank M., Bjorak G. and Semiletov I. (2009) The distribution of neodymium isotopes in arctic ocean basins. *Geochimica et Cosmochimica Acta* **73**(9), 2645–2659.

Ritz S. P., Stocker T. F. and Joos F. (2011) A coupled dynamical ocean-energy balance atmosphere model for paleoclimate studies. *Journal of Climate* **24**(2), 349–375.

Roberts N. L., Piotrowski A. M., McManus J. F. and Keigwin L. D. (2010) Synchronous deglacial overturning and water mass source changes. *Science* **327**(5961), 75–78.

Sarmiento J. L. and Gruber N. (2006) *Ocean Biogeochemical Dynamics*. Princeton University Press.

Sarmiento J. L., Thiele G., Key R. M. and Moore W. S. (1990) Oxygen and nitrate new production and remineralization in the North Atlantic subtropical gyre. *Journal of Geophysical Research* **95**, 18,303–18,315.

SCOR Working Group: (2007) Geotraces – an international study of the global marine biogeochemical cycles of trace elements and their isotopes. *Chemie der Erde – Geochemistry* 67(2), 85–131.

Sholkovitz E. and Szymczak R. (2000) The estuarine chemistry of rare Earth elements: comparison of the Amazon, Fly, Sepik and the Gulf of Papua systems. *Earth and Planetary Science Letters* **179**, 299–309.

Siddall M., Henderson G. M., Edwards N. R., Frank M., Müller S. A., Stocker T. F. and Joos F. (2005) 231Pa/230Th fractionation by ocean transport, biogenic particle flux and particle type. *Earth and Planetary Science Letters* **237**(1–2), 135–155.

Siddall M., Khatiwala S., van de Flierdt T., Jones K., Goldstein S. L., Hemming S. R. and Anderson R. F. (2008) Towards explaining the Nd paradox using reversible scavenging in an ocean general circulation model. *Earth and Planetary Science Letters* **274**, 448–461.

Siddall M., Stocker T. F., Henderson G. M., Joos F., Frank M., Edwards N. R., Ritz S. P. and Müller S. A. (2007) Modeling the relationship between 231Pa/230Th distribution in North Atlantic sediment and Atlantic meridional overturning circulation. *Paleoceanography* **22**, PA2214.

Tachikawa K., Athias V. and Jeandel C. (2003) Neodymium budget in the modern ocean and paleo-oceanographic implications. *Journal of Geophysical Research* **108**(C8), 3254.

Tachikawa K., Jeandel C. and Roy-Barman M. (1999) A new approach to the Nd residence time in the ocean: the role of atmospheric inputs. *Earth and Planetary Science Letters* **170**(4), 433–446.

Talley L. D., Reid J. L. and Robbins P. E. (2003) Data-based meridional overturning streamfunctions for the global ocean. *Journal of Climate* **16**(19), 3213–3226.

Tschumi T., Joos F., Gehlen M. and Heinze C. (2011) Deep ocean ventilation, carbon isotopes, marine sedimentation and the deglacial CO_2 rise. *Climate of the Past* **7**, 771–800.

Tschumi T., Joos F. and Parekh P. (2008) How important are southern hemisphere wind changes for low glacial carbon dioxide? A model study. *Paleoceanography* **23**, PA4208.

van de Flierdt T., Frank M., Lee D.-C., Halliday A. N., Reynolds B. C. and Hein J. R. (2004) New constraints on the sources and behavior of neodymium and hafnium in seawater from pacific ocean ferromanganese crusts. *Geochimica et Cosmochimica Acta* **68**(19), 3827–3843.

von Blanckenburg F. (1999) Paleoceanography: Tracing past ocean circulation? *Science* **286**(5446), 1862–1863.

Associate editor: Sidney R. Hemming